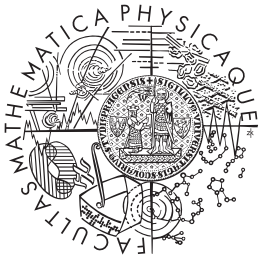

FACULTY
OF MATHEMATICS
AND PHYSICS
Charles University

HABILITATION THESIS

Dalibor Nosek

Mass Composition and Arrival Directions of the Highest Energy Cosmic Rays

Prague, March 2018

Mass Composition and Arrival Directions of the Highest Energy Cosmic Rays
Habilitation Thesis
Prague, March 2018

Dalibor Nosek

Institute of Particle and Nuclear Physics
Faculty of Mathematics and Physics
Charles University
V Holešovičkách 2
18000 Prague 8
Czech Republic

nosek@ipnp.troja.mff.cuni.cz
http://ipnp00.troja.mff.cuni.cz/∼ nosek/

Contents

1 Preface

This thesis focuses on related aspects of experimental exploration of the highest energies cosmic rays. Four recent thematically linked studies [A01, A02, B01, B02] are put into a wider context and commented in detail. The presented analysis methods were received with the help of data gathered by the Pierre Auger Observatory while studying the mass composition and arrival directions of primary cosmic particles.

The motivation to address these issues came from the fact that, in spite of a large amount of collected data and great effort towards its interpretation, the properties of the most energetic cosmic particles are not yet fully understood. In the past years, the largest cosmic ray observatories precisely measured the upper end of the energy spectrum of cosmic rays and agreed on the main features of its shape. But even the average particle mass in primary beams is the subject of current debates. In addition, all findings indicate that without further input, the analyses of arrival directions of cosmic rays are not able to provide us with reliable information on where these particles traveled from and how they gained so much energy.

I first encountered the aforementioned problems when I started participating in the physics program of the Pierre Auger Observatory some time before its construction began in 2004. My preparation works included various Monte Carlo simulations of the production of muons and Cherenkov photons in extensive air showers caused by cosmic particles of the highest energies [C01, C02]. In the following years I was involved in directional analyses of cosmic ray data collected at the Pierre Auger Observatory. The main benefit of this project was a way of assessing the properties of signals detected in the directions of specific objects. Besides other results [C03, P03, P04, P05, P06, P23], I focused on the description of various aspects of the observed accumulation of the highest energy events with arrival directions pointing to the vicinity of Centaurus A [P02, P09, P10, P20, P30], the nearest active galactic nucleus. As a first step going beyond traditional approaches [P16], I dealt with the time variability of signals from a given source [C08, C09, C10]. Finally, we proposed a nontrivial description of a source signal immersed in an unknown background. For this we assumed that predefined source properties are derived from previous observations or are set based on model considerations [B01, B02]. This strategy allows us to store various types of information obtained from measurements with the ability to make predictions and compare different observations.

Initial attempts to combine directional analyses with mass-related observables [P11, P12, P13, P14] and continuing complications inherent in directional studies [P15, P17, P18, P22] resulted in my exploration of the mass composition of primary cosmic particles. This work took place on several levels. Firstly, I was involved in studies that were aimed to employ different components of extensive air showers in order to check, refine and eventually complement the hitherto utilized mass-related observables. In this context, various experimental [P25, P29] as well as numerical [C06, C07, C11, C12] analyses were carried out. In particular, we defined a simple mass observable that allows us to estimate the spread of the primary beam

of the highest energy cosmic particles [A01]. Secondly, I started to work on using of sufficiently verified aspects of hadronic processes, applied in the development of extensive air showers, with the view of providing alternative ways how to interpret mass-sensitive observables [C05, P26, P27]. In this case, average values of mass-related observables were utilized while minimizing the impact of as many external assumptions as possible [A02]. Maximum entropy solutions for mixing fractions of primary masses were shown to have the capacity to assess basic properties of hadronic interactions at ultra-high energies.

The results summarized in this thesis are backed by various analyses I made, presented and discussed within the Pierre Auger Collaboration, see the lists of internal reports [P01]-[P30]. These works helped in various ways in discussions during preparation of directional [24, 25] and compositional studies [67, 92] submitted later by the collaboration. Interesting results were summarized in conference contributions [C01]-[C12]. Some of them were inspired by my participation in the physics program at the Cherenkov Telescope Array Project, when studying the time variability of very high energy γ-ray emitters. Most recent results were published in Refs. [A01, A02, B01, B02]. They include the methods for the analysis of cosmic ray data that were worked out in the cooperation with my colleagues. Our studies are well separable from my collaborative activities since, in some aspects, they bring forth original perspectives on the issues addressed.

The presented work is organized as follows. In the review part, Section 2 provides a brief introduction to the topic of cosmic rays and extensive air showers emphasizing the current issues. The Pierre Auger Observatory is described in Section 3, together with basics of data processing. The following two sections present my original contributions, including comprehensive information about cosmic ray physics treated in a simplified manner, and a description of related results obtained at the Pierre Auger Observatory. In Section 4, I describe the composition problem [A01, A02] and ways it can be addressed with the help of observables obtained from extensive air showers. Section 5 deals with the directional analysis of cosmic rays [B01, B02] in the context of their propagation through the cosmic space from their possible sources to a detector on Earth. Each of the latter two sections is accompanied by my commentary on the papers which are reprinted in Appendices. In order to clarify my additional activities related to the topics discussed, the three separate lists of references, beginning on pages 51, 52 and 54, respectively, summarize different types of the publications to which I contributed significantly. Finally, Section 6 lays out a brief summary of this thesis.

2 Challenges in cosmic ray physics

Cosmic rays (CR) are generally understood as charged nuclei that originate outside the solar system. They remain one of the most extreme example of the departure of matter from a state of thermal equilibrium. The total energy of these particles was measured to span from about an energy of 1 GeV to over to 100 EeV. The rate with which the most energetic particles, those with energy above 10 EeV, hit the Earth's atmosphere is less than one particle per km^2 per year (one particle per m^2 per year at the PeV range). The CR flux falls so rapidly with energy that above an energy of 1 PeV it becomes impractical to make direct measurements. Such CRs interact with nuclei in the Earth's atmosphere and produce extensive air showers (EASs) of secondary particles. The scatterings that these secondaries undergo through interactions with the material of the Earth's atmosphere spread them over a significant area at the level of observation. Typically around 10^{11} secondary particles cover approximately 10 km^2 for air showers initiated by a proton with an energy of 10 EeV (some 10^6 shower particles are spread over about 10^4 m^2 at the PeV range).

The ultra-high energy cosmic rays (UHECRs)[1] are registered through the manifestations of secondary EAS particles in detectors with giant aperture. Such devices include large ground-based arrays of detectors recording secondary shower particles. Another way is to use telescopes registering the light that occurs during the passage of secondaries through the Earth's atmosphere. The largest hybrid detector that combines both independent techniques of detection is currently operating at the Pierre Auger Observatory (PAO). The hybrid data are collected with roughly 1/10 statistics by the Telescope Array experiment, located at the northern hemisphere.

In spite of a number of important results, the main conclusion of the experimental effort done in the past years is that there is still insufficient data to answer all the questions concerning the origin and nature of cosmic particles which so rarely strike the Earth's atmosphere and have such enormous energies. Achieving this goal involves the observation of the CR energy spectrum, mass composition and distribution of arrival directions, all three of which need to be interpreted in a consistent manner. The relevant issues of the UHECRs are discussed in many reviews, for example in Refs. [1, 2, 3, 4, 5, 6].

The first key to understanding all the CR problems is the shape of the energy spectrum, for more details about different measurements and their interpretation see Ref. [5]. A power law behavior of the CR flux was measured over ten orders of magnitude. That the energy spectrum flattens above about 5 EeV, in the ankle region, was inferred from observations made with the first large shower arrays. Recently, a steepening in the CR spectrum at about 40 EeV has been confirmed by the largest experiments. Nowadays, the CR flux at this energy range is measured

[1] In this thesis, ultra-high energy cosmic rays are defined as those cosmic particles that have energies above 1 EeV = 10^{18} eV. Cosmic particles with energies over 40 EeV, around which a steep suppression of the CR flux is measured, are sometimes referred to as extreme energy cosmic rays.

with unprecedented accuracy [7, 8, 9]. However, it is unclear what causes the ankle feature. Also, it is not known whether the observed steepening is a consequence of a limit to which sources can accelerate particles or whether this is a cosmological effect caused by the interaction of CRs with the cosmic microwave background (CMB) predicted by K.Greisen [10], G.T.Zatsepin and V.A.Kuzmin [11] (GZK effect).

Closely connected with the spectral characteristics, knowledge of the mass composition of UHECRs is crucial for a correct interpretation of their origin, acceleration and propagation through the universe. For example, if the ankle feature in the energy spectrum (about 5 EeV) and the sharp decline in the CR flux at around 40 EeV are associated with the propagation of CRs and their interactions with the CMB, these particles should be light in a wide energy range [12, 13]. On the other hand, the primary CR masses should rise above the ankle energies if these phenomena are linked with the ability of sources to accelerate cosmic particles [14, 15, 16]. In addition, consideration should be given to the transition between the Galactic and extragalactic components of the CR flux [14, 15], which probably takes place just below or in the ankle range. Accurate verification of these options, however, is still hampered by the impossibility of direct mass measurements. Only mass distributions are currently inferred for primary CR beams with energies mostly below 40 EeV, just above which the impact of point sources should be recognized.

A detailed understanding of how a shower of secondary particles develops in the Earth's atmosphere is important for learning anything about the type and energy of a cosmic particle that caused this shower. Data from the LHC helps but, at most of the energies of interest ($E > 1$ EeV), the description of nuclear collisions, including the issues of cross section, inelasticity and multiplicity, is still imprecise, thus possibly affecting the mass-related analysis. On the other hand, UHECR experiments provide new data for testing models of hadronic interactions [17, 18]. Currently, the excess of muons measured in the EASs, and related observations, are considered to be the key inputs for a better description of shower development [18, 19] or, at least, for allowing for a first order assessment of the self-consistency in EAS modeling.

Despite various analyses, it is still a mystery where the most energetic particles originate from. New experimental data, the absence of photons and neutrinos with ultra-high energies, indicates that the highest energy CRs are not products of decay or annihilation of unknown exotic particles [20, 21]. The CRs are rather maintained in specific acceleration regions by a magnetic field where the energy is supplied to them gradually. Such objects could be identified using a sufficiently large set of directional data, if there are not too many CR sources located not far from the Earth. Linear dimensions and magnetic fields of these candidates should correspond to the Larmor radius for the accelerated particles. However, although a large amount of information has been accumulated and analyzed [22, 23, 24, 25], there is no experimental evidence directly indicative of possible point sources of UHECRs. The main problems are unknown types of arriving CRs, energy losses during their propagation to a detector on Earth and unknown structures of intervening magnetic fields.

In this context, it is important noting that the PAO has recently reported an indication that arrival directions of events with energy above 8 EeV are not distributed isotropically on the whole observable sky, whilst no deviation from isotropy has been observed in the 4-8 EeV range [26]. This result, captured in the dipole scale, was confirmed independently in the angular power and needlet analysis using more than 110000 events (total exposure of 76800 $\mathrm{km^2 \cdot sr \cdot yr}$) [26]. The direction of the dipole points out of our Galaxy. Since the magnitude of the dipole is much larger than the one resulting from the peculiar motion of the Earth, this finding indicates an extragalactic origin of a certain amount of UHECRs [27]. The size of the observed excess is probably conditioned by the passage of extragalactic particles through structures in the Galaxy and its halo. In any case, we have now an observation-based rationale for searching for the sources of the highest energy cosmic rays outside of our Galaxy, hitherto considered as plausible but unconfirmed. Accordingly, the measured energy spectrum, mass composition and angular distribution of the most energetic cosmic rays are to be shaped coherently by the effects of their propagation in the extragalactic medium as well as in the Galactic environment, but still respecting specificities of their production.

3 The Pierre Auger Observatory

The Pierre Auger Observatory (PAO) is located in the Pampa Amarilla region of the province of Mendoza, near town Malargüe, Argentina, between latitudes 35.0° and 35.3° S and between longitudes 69.0° and 69.4°. The PAO detectors are at altitudes between 1340 and 1610 m above the sea level, corresponding to an atmospheric overburden of about 875 g·cm^{-2} on average.

The PAO is based on the hybrid concept. Both independent detector systems, surface stations and fluorescence telescopes, are combined to detect secondary particles from showers caused by CR primaries in the Earth's atmosphere. The surface detector (SD) operates continuously, registering charged particles and photons hitting the ground. At its periphery, the fluorescence detector (FD) records the EAS development via the amount of nitrogen fluorescence generated by the passage of charged particles through the air during dark nights and under favorable conditions.

In this section, only relevant information is given. The layout of the PAO is shown in Fig.1. A detailed description of the detectors and additional equipment installed at the PAO and of data acquisition and processing can be found in Refs. [28, 29].

3.1 Surface detector

The SD is composed of a baseline array, comprising 1600 water Cherenkov stations placed in a triangular grid with nearest neighbors separated by 1500 m over a flat area of about 3000 km^2. It is complemented by an array of 61 water Cherenkov stations covering 23.5 km^2 on a 750 m grid (Infill array). The SD has a 100% duty cycle and an energy independent geometrical aperture ($\propto \cos\theta$ where θ denotes the zenith angle) above trigger saturation at energy of 3 EeV for the baseline array (0.3 EeV for the Infill array). The coverage is largely uniform in right ascension.

Each of the surface stations contains 12 t of water. They are equipped by three photomultiplier tubes that register Cherenkov light initiated by passing particles with high velocities. The device registers secondary electrons, photons and muons from air showers. A vertical muon with energy of 1 GeV deposits an energy of about 240 MeV passing the tank. An average electron deposits a few tens of MeV in the tank. The unit for the shower signal is a vertical equivalent muon (VEM). The large sensitivity to muons and the height of the individual tanks (1.2 m) allows the surface array to have an excellent sensitivity to horizontal showers ($\theta > 60°$).

The shower signal is sampled at a rate of 40 MHz. Timing information is obtained from GPS receiver. The absolute time resolution is about 10 ns. By sampling the times and sizes of signals, the shower geometry, the shower size and the arrival direction of the incident cosmic ray are determined. The analysis of the time structure of signals allows to identify the pulses from individual muons and to determine the rise time of deposited signals. These characteristics are used to construct observables sensitive to the type of primary particle, thus making it possible to distinguish showers caused by neutrinos from showers initiated by photons and nuclei.

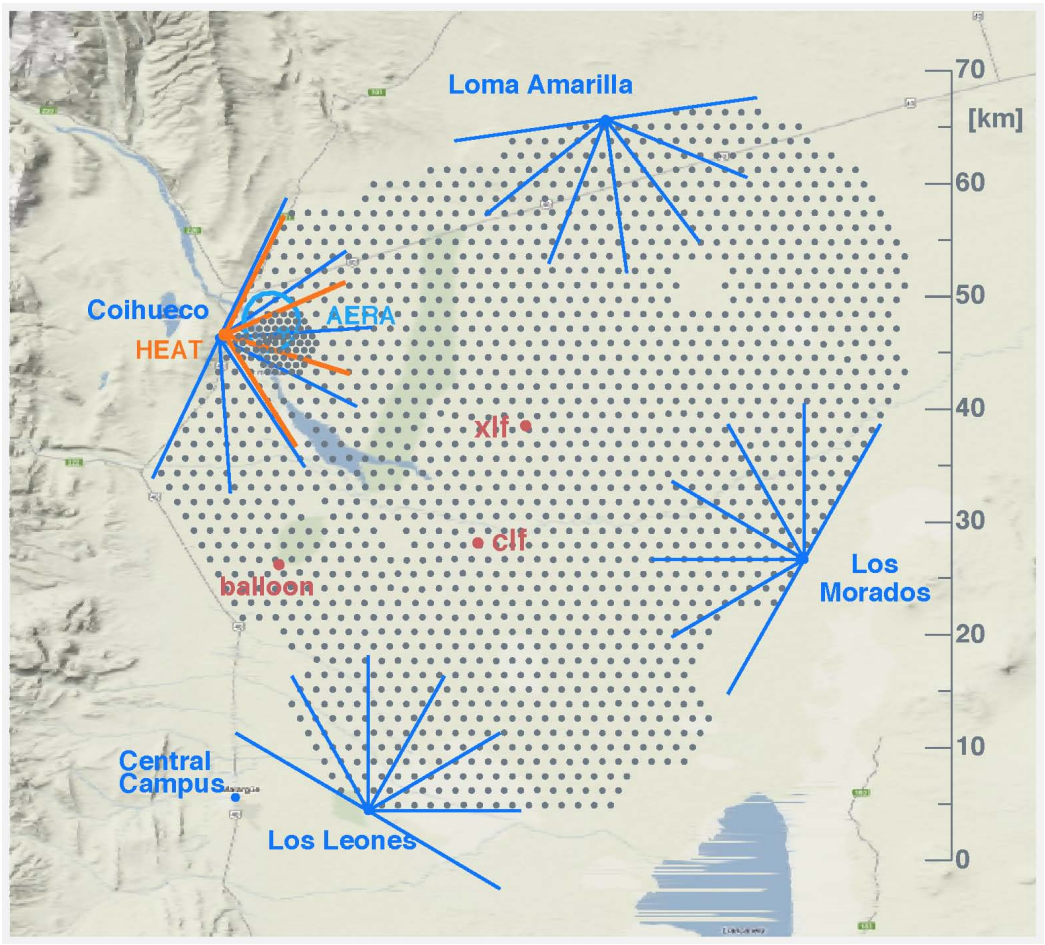

Figure 1: The Pierre Auger Observatory. Grey dots correspond the 1660 stations of the surface detector. The four fluorescence detector enclosures are shown, each with six telescopes. Also shown is the Infill array, three fluorescence telescopes with a higher elevation angle (HEAT) and stations registering radio signals (AERA). The two laser facilities, CLF and XLF, are located near the center of the surface array. Also shown is a balloon launching station for monitoring atmospheric profiles. Taken from internal Auger websites.

3.2 Fluorescence detector

The FD installed at the PAO is composed of 24 telescopes distributed in four sites at the periphery of the SD array. Each telescope has a field of view of $30^\circ \times 30^\circ$ in elevation and azimuth from 1.5° to 30° above the horizon. A set of six telescopes in each site covers 180° in azimuth. This geometrical arrangement ensures full detection efficiency for hybrid showers in excess of an energy of 10 EeV evolved over the SD. Three additional High Elevation Auger Telescopes (HEAT), installed near one FD site, share in a horizontal position the same field of view as the original fluorescence telescopes. Tilted upward by 29°, the additional telescopes enlarge the elevation coverage to 60° for air showers of lower energies from 0.1 EeV to 1 EeV.

Each FD telescope collects the light from an air shower over an aperture of 3.8 m^2. Their optical system is composed of an entrance filter and corrector ring which minimize spherical aberrations of the shower image. After being reflected by a mirror with a diameter of 3.6 m, the collected light illuminates a camera composed of 440 photomultiplier tubes, each with a field of view of about $1.5° \times 1.5°$. The telescopes operate during dark and clear enough nights with a duty cycle of 13%.

The FD allows detection of the ultraviolet fluorescence light induced by the energy deposit of charged shower particles in the Earth's atmosphere. The fluorescent light is emitted isotropically along the air shower and can be detected tens of kilometers away. Since the light is emitted proportionally to the number of shower electrons, and remain nearly unaltered during its propagation through the atmosphere, its time profile reflects well the longitudinal evolution of the electromagnetic cascade. This allows for measurements of composition sensitive observables such as the depth where the number of shower particles reaches its maximum.

3.3 Enhancements

The ongoing upgrade of the PAO detectors is aimed to provide a high statistics sample of events with primary energy and mass information [30]. Each of SD stations will be equipped with a 4 m^2 surface scintillator detector installed on the top of the existing water Cherenkov stations [31]. Due to a different response to the electromagnetic and muonic components, this equipment will be able to disentangle both kinds of EAS signal, providing thus estimates on an event-by-event basis.

The AMIGA enhancement (Auger Muon and Infill for the Ground Array) will be used to verify methods for extracting muon information from the upgraded SD array [32]. It is a joint system of 61 water Cherenkov stations with 750 m spacing (Infill Array) accompanied by buried plastic scintillator counters. Scintillators composed of three highly segmented 10 m^2 modules are placed 2.3 m underground, imposing an energy cutoff for vertical muons of about 1 GeV.

Co-located with the Infill array, the Auger Engineering Radio Array (AERA) is currently tested [33]. The main goal of this equipment is the investigation of the radio emission from EASs and the provision of other shower observables at the energy range around 1 EeV. An additional program is pursued in order to determine whether a detector sensitive to microwave background radiation produced by the scattering of low energy electrons in the weakly ionized plasma along shower evolution would be a suitable alternative for the study of UHECRs [34].

Atmospheric conditions need to be known with sufficient accuracy for the FD reconstruction of air showers. The two laser facilities, Central Laser Facility (CLF) and eXtreme Laser Facility (XLF), are installed at central positions within the SD array for obtaining profiles of the aerosol optical depth [35]. Infrared cameras and lidar systems are used to detect clouds [29]. An optical telescope FRAM (ph(F)otometric Robotic Atmospheric Monitor) measures starlight to determine the wavelength dependence of Rayleigh and Mie scattering of light in the atmosphere [36].

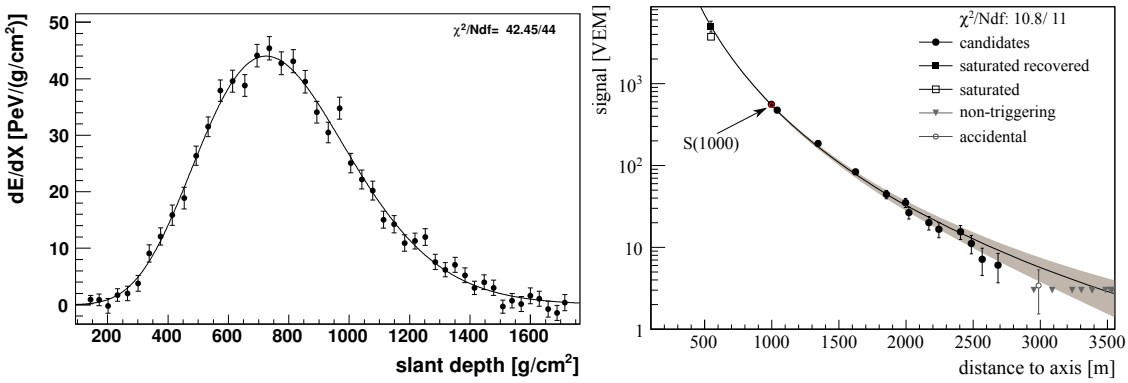

Figure 2: Left: Energy deposited in the atmosphere is shown as a function of slant depth. Right: Shower size is depicted as a function of distance from the shower core. Taken from Ref. [29].

3.4 Processing of events

The essential feature of the PAO is its hybrid design, in which UHECRs are detected simultaneously by water Cherenkov stations (Section 3.1) and by fluorescence telescopes (Section 3.2). The FD telescopes always operate in conjunction with the SD array. This option enables us to overcome some limitations of individual techniques of detection thus providing us with high-quality data.

The FD records the shower development in the Earth's atmosphere and yields a nearly calorimetric measurement of the cosmic ray energy. The FD data is primarily used for the energy calibration of the SD array, but it also provides us with mass-sensitive observables. Up to now, about 17000 high quality events with energies 0.2 EeV $< E <$ 1.3 EeV and about 26000 ones with energies $E > 0.6$ EeV have been collected by the high elevation (HEAT) and standard FD telescopes, respectively.

The SD array responds to the electromagnetic and muonic components of the shower, independently of FD measurements. Its large exposure allows to measure effectively the UHECR flux with a minimal input from models of hadronic interactions (Section 5.2). A shower falling into the SD array is detected with 100% efficiency for energies over 3 EeV, regardless of the mass of primary particle causing the shower. In total, almost two hundred thousand good quality SD events with energies exceeding 3 EeV have been registered from January 2004 to May 2017. Out of these events, about 17000 (570) events with energies over 10 EeV (40 EeV) have passed the standard reconstruction.

3.4.1 Hybrid measurements

The hybrid reconstruction of air shower is based on FD data with additional timing information from the SD. With this data the shower geometry is found and light attenuation from the shower to the FD telescope is estimated based on a fluorescence yield in air [37]. The longitudinal profile of the EAS is determined by observing the

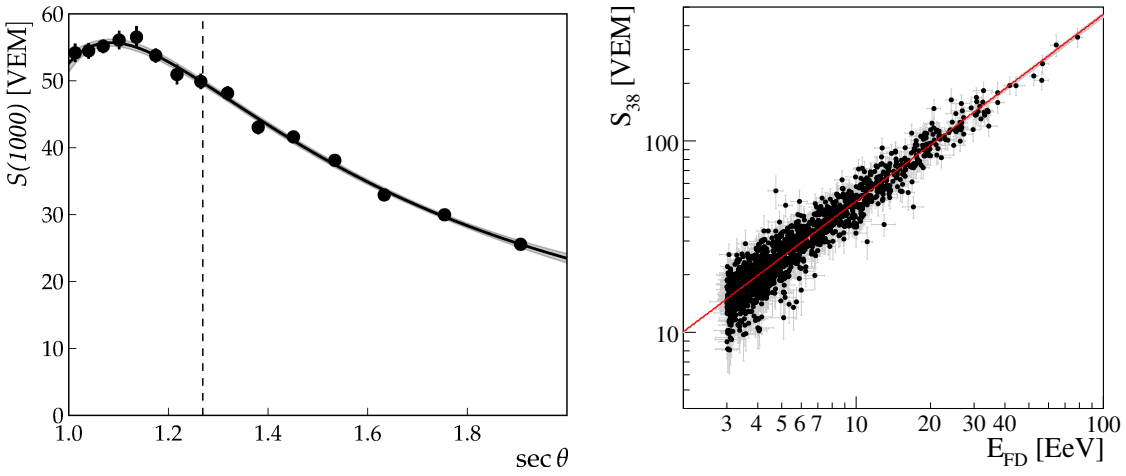

Figure 3: Left: Attenuation curve, $S(1000)(\theta)$, for the CIC method. The dashed vertical line indicates the S_{38} signal (sec(38°) ≈ 1.27). Right: Calibration curve for the surface detector. The shower size, S_{38}, measured by the SD array is shown as a function of calorimetric energy, $E_{\rm FD}$, measured by the FD. The 1475 high quality hybrid events are depicted. Taken from Ref. [29].

fluorescent light emitted by nitrogen molecules which are excited by passing charged shower particles through the atmosphere. The profile of the energy deposit, assumed as a function of a slant depth X, is reconstructed using a Gaisser-Hillas function [38]

$$\frac{\mathrm{d}E}{\mathrm{d}X}(X) = \left(\frac{\mathrm{d}E}{\mathrm{d}X}\right)_{\rm max} \left(\frac{X - X_0}{X_{\rm max} - X_0}\right)^{\frac{X_{\rm max}-X_0}{\lambda}} e^{\frac{X_{\rm max}-X}{\lambda}}, \qquad (1)$$

where X_0 and λ are parameters, and $X_{\rm max}$ is the depth of shower maximum. The example of the energy deposit is shown in the left panel in Fig.2 as a function of the atmospheric thickness traversed by a shower (slant depth X).

A calorimetric estimate of primary energy, $E_{\rm FD}$, is obtained from the fluorescence profile of a shower by integrating Eq.(1), while correcting for an invisible energy carried away by shower muons, neutrinos and hadrons with the help of Monte Carlo simulations. Currently, the total systematic uncertainty for the energy reconstruction is about 14%. Fuller details about accuracy of measurements are in Ref. [29].

The depth of shower maximum, $X_{\rm max}$, determined from the measured profile of the energy deposit in the air is well suited for estimating the mass composition of primary CR beams (Section 4.1.1). For better accuracy, only those $X_{\rm max}$ values are accepted in the analysis that fall into the field of view of the FD telescopes. Uncertainties of $X_{\rm max}$ data are given by the detector effects (light collection, alignment of telescopes, timing information etc.) and by the precision to which the actual density profile of the Earth's atmosphere and its impurities are known. The total resolution of the depth of shower maximum better than 25 g·cm^{-2} (15 g·cm^{-2}) at 1 EeV (10 EeV) is achieved after a number of necessary quality limitations [39].

3.4.2 Surface array observations

The sizes and times of signals from an air shower registered by the ground-based SD stations are utilized to measure the energy and arrival direction of an incident cosmic particle. In order to guarantee good data quality, only events are accepted that have the SD station with the highest signal surrounded by six operating neighbors' stations (a working hexagon). This option assures an accurate estimate of the impact point of the shower on the ground allowing also for a simple geometrical calculation of the SD exposure.

The size of the signal at a distance of 1000 m from the shower core, $S(1000)$, is used to estimate the energy of primary cosmic particles. For this purpose, the lateral distribution of the signal size registered in the ground stations, as displayed in the right panel in Fig.2, is fitted with a modified function of Nishimura, Kamata and Greisen (NKG) [40, 41]

$$S(r) = S(1000) \left(\frac{r}{r_{1000}}\right)^{\beta} \left(\frac{r + r_1}{r_{1000} + r_1}\right)^{\beta+\gamma}, \tag{2}$$

where r is the distance from the shower core, $r_{1000} = 1000$ m is the optimal distance for stations in the SD array and $r_1 = 700$ m. The parameter γ is near 0. The parameter β depends on the zenith angle and shower size. The uncertainty with which the parameter $S(1000)$ is reconstructed decreases with increasing shower energy. It is about 12% for showers with energies above 10 EeV.

In the left panel in Fig.3, the measured attenuation curve of the ground signal and its approximation are shown as functions of zenith angle. This dependence is given by the fact that the shower with a larger zenith angle must pass through a larger amount of air before it hits the ground (Section 4.1.2). To correct this effect, a Constant Intensity Cut (CIC) method is adopted, assuming an isotropic flux of primary particles hitting the Earth's atmosphere [29]. In practice, an energy estimator S_{38} is constructed for each shower. It corresponds to the ground signal caused by a primary particle with a given energy that would come into the SD array with a zenith angle of about 38°, representing the median zenith for the isotropic distribution, when zenith angles $\theta \in \langle 0°, 60° \rangle$.

Hybrid events registered simultaneously by both FD and SD detector systems are used to estimated the cosmic ray energy measured by the SD array [28]. Only events which meet a number of quality and accuracy conditions and have well determined FD energies, in particular, are taken into account for the energy calibration. The resulting calibration curve, depicted in the right panel in Fig.3, is [28]

$$E_{\mathrm{FD}} = A \, (S_{38}/\mathrm{VEM})^{B}, \tag{3}$$

where $A = (0.190 \pm 0.005)$ EeV and $B = 1.025 \pm 0.007$. This construction is only slightly model dependent. The energy resolution of the SD is about 16% for lower energies ($E \approx 3$ EeV) and about 12% for the highest energies ($E > 40$ EeV) [29].

Another method for the energy estimate is used for events caused by inclined showers with zenith angles exceeding 60°, the footprint of which is registered by the SD array, see Ref. [42]. The same work describes the method that is applied for the energy estimate of CR events detected by the Infill array.

The arrival direction of a cosmic particle causing an extensive air shower is obtained by fitting start times of signals in the SD stations to the approximate evolution of the shower front. Along with this information, the shower impact point estimated from the lateral distribution of the SD signals is used to obtain a shower axis. The accuracy of this procedure depends on the number of involved SD stations. The angular resolution achieved for events with more than three (six) stations is better than 2° (1°) for energies in excess of 10 EeV, and it is improving with increasing zenith angle. Hence, less strict constraints are usually adopted for the number of neighboring SD stations with signals registered from a single air shower when directional analyses are conducted at the highest energy range (Section 5.3). The angular accuracy for events registered with the SD array and related topics are discussed in Ref. [43].

The mass-sensitive observables can also be inferred from a large sample of SD data over a wide range of energies. These observables yield information complementary and independent of the FD data, allowing for deeper testing of the existing models of hadronic interactions, for more details see Section 4.2. Firstly, distributions of the muon production depth can be obtained from timing information recorded by the SD stations far from the shower core. Useful information about the primary mass composition is then inferred from the depth along the shower axis where the production of muons reaches maximum. Due to the increase in the number of shower muons with primary energy (Section 4.1.2), the uncertainty of this observable ranges from 100 g·cm^{-2} at lower energies to about 50 g·cm^{-2} at the highest energies. Secondly, the depths of shower maximum can be inferred by using a method of measuring the rise time of signals registered in the SD stations. A useful mass-related SD parameter is obtained by subsequent calibration with the FD data. The resolution in this measurement of X_{max} is about 45 g·cm^{-2}. In addition, the azimuthal asymmetry in the rise time of SD signals is utilized to provide a novel observable sensitive to the primary mass composition. Further details about muons in air showers and about the measurement and interpretation of their production depth are summarized in Ref. [44]. The concept of the rise time, its measurement and mass-sensitive abilities are described in details in Refs. [45, 46].

4 Mass composition

Indirect measurements of the mass composition of the primary CR beams are conducted by detecting secondary particles in showers that UHECRs initiate in the Earth's atmosphere. The mass composition can be inferred from the longitudinal development of showers using fluorescence or Cherenkov telescopes or from the distribution of signals caused by secondary particles in surface detectors (Section 3). Improvements in the measurement of EAS profiles brought about by a hybrid technique of detection at the PAO have significantly reduced the reconstruction uncertainties in mass-sensitive observables. Furthermore, unique data on electromagnetic and muonic components of extensive air showers will soon be available from the upgraded SD array at the PAO. Such measurements are expected to distinctly refine our knowledge of EAS physics.

In order to interpret shower observables in terms of primary masses, we mainly rely on models of hadronic interactions. Currently, there are no definitive conclusions since we are in a situation when mass-related data is more accurate than reported discrepancies between existing model predictions, see Section 4.2.

In this section, the main focus is given to the issues related to the primary CR composition at ultra-high energies. The basic features of extensive air showers are described relying on simple phenomenological considerations. Suitable mass-sensitive observables are introduced in Section 4.1. Available experimental data obtained at the PAO are presented in Section 4.2. Its interpretation and possible implications are briefly discussed. In Sections 4.3 and 4.4, the results obtained by the author and his collaborators are summarized, emphasizing the main points and putting them into context. The two original papers [A01, A02] are reprinted in Appendices A and B.

4.1 Extensive air showers

The basic features of cascades of secondary particles that follow the interaction of primary CRs with nuclei in the Earth's atmosphere are well understood within a simplified model. Such a model designed to describe an electromagnetic shower was originally suggested by Heitler [47, 48]. Characteristics of the hadron component and relevant observables are described in its extended version [49, 50, 51].

More accurate information on the development of a cascade of secondary particles in the air is obtained using Monte Carlo simulations. However, at the highest energies, the modeling of hadronic interactions is not optimal since it relies on extrapolations of accelerator measurements and, hence, introduces considerable uncertainties in the interpretation of UHECR data. Different shower characteristics are differently sensitive to the energy dependence of the cross section, multiplicity and elasticity of hadronic collisions [52, 53, 54]. It implies, on the other hand, that UHECR data can be used to study properties of hadronic interactions at energies much larger than currently available in ground-based accelerators, see e.g. Refs. [17, 18].

Comprehensive description of the composition problem and related issues can be found, for example, in Refs. [2, 3, 6]. The techniques for determining the mass composition of primary UHECRs in different experiments are discussed and compared with each other in Refs. [55, 56, 57].

4.1.1 Electromagnetic component

Useful information on the primary particle causing a shower is stored in the longitudinal profile of the cascade of secondary particles produced in the Earth's atmosphere. In this respect, the atmosphere acts as a calorimetric device which allows the development of secondary cascades and simultaneously enables us to detect them due to the production of fluorescent light or Cherenkov radiation.

In the first inelastic interaction of a primary particle with an atmospheric nucleus, and in each consecutive hadronic interaction, about one third of the incident energy is transferred from the hadronic component to the electromagnetic component of the shower via decays of neutral pions into photons, followed by the production of electrons and positrons. Charged hadrons carry away the rest of the primary energy. The energy transfer continues until the decays of charged hadrons prevail over their interactions with atmospheric nuclei. In a first order approach, the mean interaction path for charged pions and the multiplicity of hadronic interactions are independent of the pion energy. If, on average, the charged hadrons start to decay after n collisions, the calorimetric energy (Section 3.4.1) stored in the electromagnetic component of the EAS induced by a cosmic particle of primary energy E is [3]

$$E_{\rm cal} = E\left[1 - \left(\frac{2}{3}\right)^n\right]. \tag{4}$$

Hence, the calorimetric energy is larger, the longer the charged hadrons reduce their energy in subsequent hadronic interactions.

Since typically $n > 5$ for primary energies above 1 EeV and not too large zenith angles ($\theta \leq 60^\circ$), most primary energy is observed in the electromagnetic component of the EAS. For example, the primary proton with an energy of about 1 EeV incident perpendicular to the Earth's atmosphere produces, at the sea level, approximately 10^{10} particles with energies above 100 keV. Among them, in the induced electromagnetic cascade, photons and about 6 times less electrons and positrons with energies 1-10 MeV account together for about 99% secondaries and carry away about 85% of the primary energy. In addition, produced in subsequent hadronic interactions, charged pions and secondary muons from their decays with average energies around 1 GeV possess about 5% and 10% of the primary energy, respectively. Much fewer neutrinos and baryons are produced during the EAS development.

The electromagnetic cascade of electrons, positrons and photons continues until the energy of each particle falls below the critical energy ϵ_γ (in air $\epsilon_\gamma \approx 84$ MeV), when bremsstrahlung and ionization energy losses for electrons (positrons) equalize approximately. At this stage of the EAS development, the cascade initiated by a

primary with energy E reaches its maximum number of particles, $N_{\max} \approx \frac{E}{\epsilon_\gamma}$. The corresponding slant depth in the atmosphere, $X_{\max}$, represents a useful variable for composition studies. At this depth, the most secondary particles are observed and, almost equivalently, the maximum energy from the shower is deposited in the air.

The development of the number of particles in the induced electromagnetic cascade is traditionally described as a function of traversed air mass, X, that is given by the density of air integrated along the path of the shower in the Earth's atmosphere. In the following, it is shown how the depth of shower maximum where the number of shower particles reaches its maximum, $X_{\max}$ (Section 3.4.1), is related to the mass of the primary particle that caused the shower. However, due to fluctuations in the shower development, the primary mass cannot be measured on an event-by-event basis. It can be inferred statistically from the distribution of the depth of shower maximum using a collection of showers with nearly the same energy.

Assume a primary proton of energy E inducing an electromagnetic cascade in the Earth's atmosphere via neutral pions created in the first or main interaction. Within the Heitler model [48], the mean depth of shower maximum is given by [3]

$$\langle X^{\mathrm{p}}_{\max} \rangle = \langle X_{\max} \mid A = 1 \rangle \approx \lambda + X_{\mathrm{r}} \ln \left(\frac{\kappa E}{2 M \epsilon_\gamma} \right). \tag{5}$$

Here, $X_{\mathrm{r}} \approx 37$ g·cm^{-2} is the radiation length in air, $\kappa = \frac{E_1}{E}$ denotes the elasticity of the first or main interaction where E_1 is the highest energy of secondaries, and a factor 2 accounts for the decay of neutral pions into two γ photons. In the first interaction, the average energy of produced hadrons, $\frac{E}{M}$, is given by the average multiplicity of hadron collisions, M. The proton interaction length λ, multiplicity M and elasticity κ of the collision depend on the primary energy.

The slope in changes of the mean depth of shower maximum, when expressed as a function of the logarithm of the primary proton energy, is [3]

$$d = \frac{\mathrm{d}\langle X^{\mathrm{p}}_{\max} \rangle}{\mathrm{d} \ln E} \approx X_{\mathrm{r}} (1 - B_\lambda - B_M), \tag{6}$$

where $B_\lambda = -\frac{\lambda}{X_{\mathrm{r}}} \frac{\mathrm{d} \ln \lambda}{\mathrm{d} \ln E}$ and $B_M = \frac{\mathrm{d} \ln M}{\mathrm{d} \ln E}$, while the elasticity in the first collision is assumed independent of the primary energy. The elongation rate, $D = d \ln 10$, characterizes the increase of the depth of shower maximum with a decade of primary energy. Because the hadron interaction length, λ, decreases approximately logarithmically with increasing primary energy and the number of secondary pions increases with rising primary energy ($M \propto E^\delta$ where $\delta > 0$ is a constant), the elongation rate for showers initiated by primary protons is approximately constant [3].

For a primary nucleus of the same energy E and mass A-times larger than the mass of the proton ($A \geq 1$) the superposition model is applied. The primary nucleus is understood as a set of A independent nucleons, each nucleon with an average energy of $\frac{E}{A}$. Then the mean depth of shower maximum is

$$\langle X^{\mathrm{A}}_{\max} \rangle = \langle X_{\max} \mid A \rangle = \langle X^{\mathrm{p}}_{\max} \left(\frac{E}{A} \right) \rangle \approx c + d \, \ln \left(\frac{E}{A} \right), \tag{7}$$

and it is assumed that the model parameters c and d depend on the properties of hadronic interactions. In this approach, the mean depth of shower maximum for primary nuclei grows logarithmically with their energy at the same elongation rate as for protons. For identical primary energies, nuclei cause on average shallower showers than protons, i.e. $\langle X^{\rm A}_{\rm max}\rangle \approx \langle X^{\rm p}_{\rm max}\rangle - d\ln A$.

Finally, the mean depth of shower maximum for events generated by a primary beam composed of a set of nuclei with the same energy E is given by averaging Eq.(7) over nuclear masses. For a mixed composition, this mean depth is

$$\langle X_{\rm max}\rangle = \langle\langle X^{\rm A}_{\rm max}\rangle\rangle \approx C - d\,\langle\ln A\rangle, \tag{8}$$

where $C = \langle X^{\rm p}_{\rm max}\rangle = c + d\ln E$ is the mean depth of shower maximum for protons. In this concept, the mean logarithmic mass of the primary beam, $\langle\ln A\rangle$, is directly related to the mean depth of shower maximum, $\langle X_{\rm max}\rangle$, obtained experimentally. This scheme also shows that, knowing basic features of hadronic interactions relevant to shower physics, any departure from the logarithmic increase of measured values of the mean depth of shower maximum with rising primary energy can be interpreted as a change in the mass composition of primary particles.

Besides the mean depth of shower maximum, the important observable is the variance in depth of shower maximum. It is composed of the variance of the depth traveled by a primary particle to the first or main collision and of the variance of the path of secondaries from the first interaction to the depth of shower maximum.

Assuming a simple concept introduced in Eq.(5), the variance in the depth of shower maximum for showers caused by primary protons of energy E is [3]

$$\sigma^2_p = \sigma^2({\rm X_{max}} \mid A=1) = \sigma^2_{\rm fr,0} + \sigma^2_{\rm sh,0} = \lambda^2 + X^2_{\rm r}\frac{\sigma^2_{\rm M}}{M^2} + X^2_{\rm r}\frac{\sigma^2_\kappa}{\kappa^2}, \tag{9}$$

where the first term is the variance of the depth of the first or main interaction, $\sigma^2_{\rm fr,0} = \lambda^2$, and the remaining terms account for the variances in multiplicity and elasticity giving together the variance of the shower development after the first interaction, $\sigma^2_{\rm sh,0}$. All terms in Eq.(9) depend on the primary energy.

For a primary nucleus with the same energy E we can write [A02]

$$\sigma^2(X_{\rm max} \mid A) = \sigma^2_{\rm fr} + \sigma^2_{\rm sh}, \tag{10}$$

where, within a simple model,

$$\sigma^2_{\rm fr}(E,A) \approx \phi(A)\xi(E)\sigma^2_{\rm fr,0}, \qquad\qquad \sigma^2_{\rm sh}(E,A) \approx \psi(A)\sigma^2_{\rm sh,0}. \tag{11}$$

Here, an energy dependent term, $\xi(E)$, may be estimated from experiment. The mass dependent function for the variance of the depth of the first interaction, $\phi(A)$, is estimated assuming the incident nucleus as a superposition of A nucleons with a subset of non-interacting spectators, giving $\frac{1}{A} < \phi(A) < \frac{1}{3} + \frac{1}{A} + O(A^{-2})$. The variance of the subsequent shower development can be parametrized in a naive superposition model using $\psi(A) \approx \frac{1}{A}$ which follows when averaging over participating projectile nucleons. For more details see Ref. [A02].

In case of a mixed primary composition, the total variance of the depth of shower maximum that is to be confronted with measurements at a given energy E is

$$\sigma^2_{\rm max} = \sigma^2(X_{\rm max}) = \langle\sigma^2_{\rm fr}\rangle + \langle\sigma^2_{\rm sh}\rangle + d^2\sigma^2_{\ln {\rm A}}, \tag{12}$$

where the law of total variance was used, $\sigma^2_{\rm max} = \langle\sigma^2(X_{\rm max} \mid A)\rangle + \sigma^2(\langle X_{\rm max} \mid A\rangle)$, see also Eqs.(7) and (10). The mean variances on the right hand side in Eqs.(12) are calculated over the mass numbers of primary particles. In this case, Eq.(12) shows that, with some input information from shower physics governed by hadronic interactions, the observed total variance of the depth of shower maximum, $\sigma^2_{\rm max}$, provides the variance of the logarithmic mass, $\sigma^2_{\ln {\rm A}}$, present in the primary beam.

4.1.2 Particles on the ground

Information about the primary composition can also be deduced from densities of charged shower particles on the ground. Let us consider that hadronic interactions occur when shower particles travel a path in the atmosphere corresponding to the transverse thickness of $\lambda_{\rm I}$ (the mean transverse length for a hadronic interaction). In the first order approach, we assume that $\lambda_{\rm I}$ is independent of the incident particle energy. We further assume that M secondary pions of approximately equal energies are produced in each interaction. On average, $\frac{1}{3}M$ of neutral pions immediately decay into photons, and the remaining about $\frac{2}{3}M$ charged pions further interact with atmospheric nuclei until their decays prevail over their interactions, see Section 4.1.1.

Under these simplifications, the number of consecutive hadronic interactions of charged pions, n, is estimated by comparing their mean interaction length with their mean decay length. While the mean interaction length of the charged pion, $\lambda_{\rm I}$, is treated as a constant, its mean decay length is proportional to its energy, $\lambda_{\rm D}(E_\pi, h) = \rho\gamma_\pi c\tau_\pi$, where $\rho(h)$ is the air density at height h above the ground, $\gamma_\pi = \frac{E_\pi}{m_\pi c^2}$ is the Lorentz factor of the pion with energy E_π and rest mass m_π, and c (the speed of light in vacuum) and τ_π are its velocity and lifetime, respectively.

A hadronic cascade induced by a primary particle with sufficient energy E ends, on average, after n hadronic interactions in the depth $X(h) = n\lambda_{\rm I}$ when the typical energy of charged pions ($\epsilon_\pi = \frac{E}{M^n}$) drops down in such a way that $\lambda_{\rm D}(\epsilon_\pi, h) = \lambda_{\rm I}$. Hence, the number of hadronic interactions, n, is estimated by [3]

$$nM^{-n} = \frac{h_0}{c\tau_\pi}\frac{m_\pi c^2}{E}\frac{1}{\cos\theta}, \tag{13}$$

where we put for the density of the isothermal atmosphere $\rho(h) = -\frac{{\rm d}X(h)}{{\rm d}h} = \frac{X(h)}{h_0}$ where $X(h) = X_0 \exp\left(-\frac{h}{h_0}\right)$, $X_0 \approx 1000$ g·cm^{-2} and $h_0 \approx 10$ km are parameters, and a primary particle is assumed to hit the atmosphere with a zenith angle θ.

The relationship written in Eq.(13) provides an estimate for the number of successive hadronic interactions for sufficiently large multiplicities. Typically, for a cosmic particle with primary energy above 1 EeV incident vertically, the number

of hadronic collisions $n > 5$ if the multiplicity $M < 100$. The number of hadronic collisions decreases with increasing multiplicity and zenith angle, giving the decay energy for charged pions ($\epsilon_\pi = \frac{E}{M^n}$ for $\lambda_{\rm D}(\epsilon_\pi, h) = \lambda_{\rm I}$) of a few tens of GeV. When, on average, the multiplicity of hadronic interactions grows sufficiently with primary energy (e.g. $M \propto E^\delta$ and $\delta > 1$), the decay energy, ϵ_π, slowly decreases [3].

After n hadronic interactions, when decays of charged pions prevail, the muonic component is completely decoupled from the electromagnetic one. If all charged pions decay into muons immediately after they reach the decay energy, ϵ_π, the total number of muons produced in the shower is estimated by the total number of charged secondary pions created until, on average, the n-th interaction occur [3]. Hence, for a shower initiated by a primary proton with energy E, the number of muons is

$$N_\mu^p \approx \left(\frac{2}{3}M\right)^n = \left(\frac{E}{\epsilon_\pi}\right)^\beta, \qquad \beta = \frac{\ln \frac{2}{3}M}{\ln M}. \tag{14}$$

Here, a parameter β, being slightly smaller than one, is given by the average multiplicity of hadronic interactions. For $M = 20 - 300$ one gets $\beta = 0.88 - 0.92$, for example. Note that in this approach the number of muons that reach the ground is independent of the interaction length of charged pions ($\lambda_{\rm I}$). These muons carry a total energy of $E_\mu \approx N_\mu^p \epsilon_\pi$.

For an incident nucleus with a mass number A and the same primary energy E, one gets for the number of muons from the superposition ansatz [3]

$$N_\mu^A \approx A \left(\frac{\frac{E}{A}}{\epsilon_\pi}\right)^\beta = A^{1-\beta} N_\mu^p. \tag{15}$$

The number of muons detected on the ground, which arise mainly as decay products of charged pions, may serve as an indicator of the primary mass. With increasing primary mass the shower develops higher and faster, charged pions in the cascade reach their decay energy sooner and thus augment the relative number of muons on the ground with respect to the electromagnetic component. In addition, $\frac{{\rm d}\ln N_\mu^A}{{\rm d}\ln E} \approx \beta$ follows from Eq.(15) for a constant primary composition. Thus, any deviation from this dependence indicates a change of the mass distribution in the primary beam [3].

Finally, let us consider the electromagnetic fraction in an extensive air shower at the ground level. The total number of electrons, positrons and photons on the ground (N_e^A) is attenuated with respect to their number at the depth of shower maximum ($N_{e,\max}$). A simple first order estimate gives [3]

$$N_e^A \approx N_{e,\max}\, e^{-\frac{\Delta X}{\lambda_a}}, \tag{16}$$

where $\Delta X = \frac{X_0}{\cos\theta} - X_{\max}$ is the distance from the shower maximum ($X_{\max}$) to the ground (X_0) for a shower incident with a zenith angle θ, and λ_a denotes an attenuation length for the electromagnetic component in the air. Using the superposition model [3] for a shower initiated by a primary with a mass number A and energy E,

$$N_{e,\max} = N_{e,\max}^p \approx \frac{E - E_\mu}{\epsilon_\gamma} \approx \frac{E}{\epsilon_\gamma} = A\frac{\frac{E}{A}}{\epsilon_\gamma} \approx N_{e,\max}^A, \tag{17}$$

showing that the amount of electrons, positrons and photons at the depth of shower maximum, $N_{e,\max}$, estimates the energy of the primary particle and is independent of its mass. In this approach, which is valid for energies in excess of 10 EeV, the total energy of the muonic component, $E_\mu \approx N_\mu^p \epsilon_\pi$, was neglected.

Since, at a given primary energy, the depth of shower maximum is shallower for heavier primaries (the first or main interaction is higher in the Earth's atmosphere), the number of corresponding electromagnetic particles detected on the ground is reduced more than the number of electromagnetic particles that are produced in showers initiated by lighter primaries that reach their maximum deeper in the atmosphere, i.e. $\Delta X^A > \Delta X^p$ in Eq.(16), see also Section 4.1.1. In summary, one expects $N_e^A < N_e^p$ for the total numbers of electromagnetic particles on the ground, while $N_\mu^A > N_\mu^p$ for muons, when extensive air showers initiated respectively by primary nuclei ($A > 1$) and protons with the same energy are analyzed.

4.2 Selected results and interpretation

The mass composition of a primary CR beam causing EASs is usually studied with the help of the distribution of the depth of shower maximum ($X_{\max}$ distributions), constructed for a given primary energy. Experimental values of this maximum are inferred from the FD measurements of the EAS energy deposit into the Earth's atmosphere, for more details see Section 3.4.1. Until now, considerable information about $X_{\max}$ distributions in a wide energy range (0.2 EeV $< E <$ 40 EeV) was collected at the PAO [39, 58]. The resolution of the depth of shower maximum was estimated to be better than 20 g·cm^{-2} above 10 EeV with systematic biases below 10 g·cm^{-2} [39, 58]. The total number of events in the latest analysis registered by the HEAT and the standard FD telescopes exceeded 42000 [58].

Sample values of the two lowest order central moments of the depth of shower maximum, $\langle X_{\max} \rangle$ and $\sigma(X_{\max})$, are shown in Fig.4 as functions of primary energy. The measured elongation rate (Section 4.1.1) of the FD data (left panel in Fig.4) is for all primary energies different from what would be predicted using the simple model described in Section 4.1.1 or based on the indicated models of hadronic interactions for either a pure-proton or pure-iron primary beam (about 60 g·cm^{-2} per decade of energy). More importantly, the behavior of the standard deviation of $X_{\max}$, $\sigma(X_{\max})$ shown in the right panel in Fig.4, is broadly consistent with the trend observed for the average values of the depth of shower maximum, $\langle X_{\max} \rangle$.

Recently, the PAO has also studied the air shower development using data collected by the SD array (Section 3.4.2). The mass-sensitive observables included the depth along the shower axis where the production of muons reaches maximum, as deduced from the timing information recorded by the SD stations far from the shower core [44]. Other observables related to the rise time of the SD signal were adopted for the analysis of primary masses [45, 46]. Whilst the resolution of these observables is worse than in the measurements with the FD telescopes, the SD array provides higher statistics of events because of its 100% duty cycle.

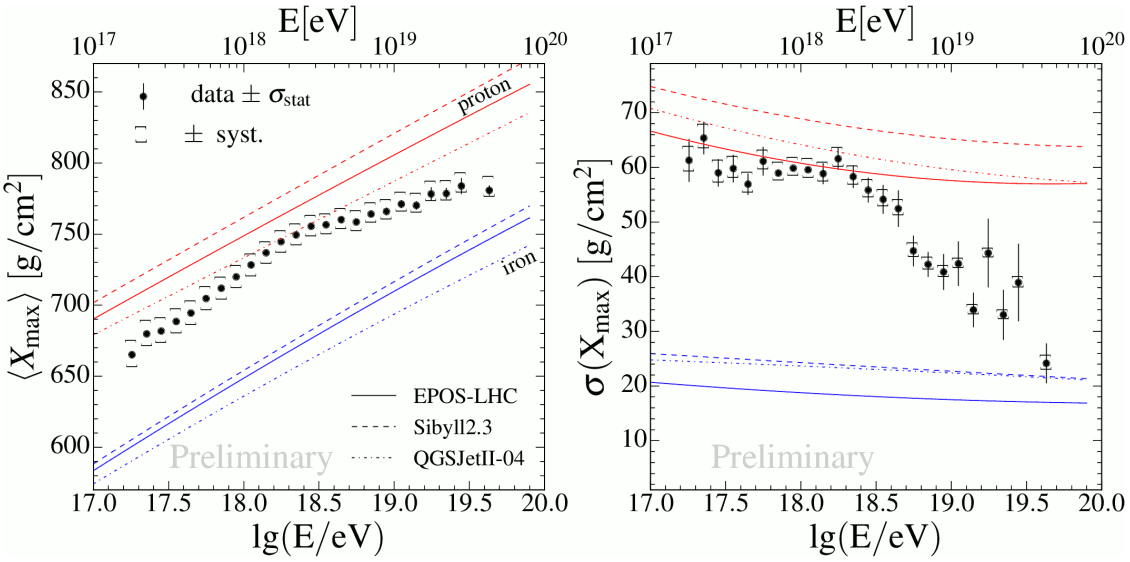

Figure 4: Energy evolution of average values (left) and standard deviations (right) of $X_{\max}$ distributions collected at the PAO are depicted as functions of primary energy. Systematic (brackets) as well as statistical (bars) uncertainties are indicated. Results of Monte Carlo simulations of air showers for proton (red) and iron (blue) primaries are shown for three models of hadronic interactions, Epos-LHC [60, 61] (full lines), QGSJet II-04 [59] (dotted lines), and Sibyll 2.3 [62, 63] (dashed lines). Reproduced from Ref. [58].

4.2.1 Mass moments

In experiments which measure the distributions of the depth of shower maximum at different energies, the average logarithmic mass in the primary beam is obtained from the average depth of shower maximum using Eq.(8). It can be achieved if the estimate of the mean depth of shower maximum for protons is known, for example, from Monte Carlo simulations based on a specific model of hadronic interactions. In a similar way, the standard deviation of the depth of shower maximum carries information on the variance of the logarithmic mass, see Eq.(12). Hence, the two lowest order mass moments, $\langle \ln A \rangle$ and $\sigma^2_{\ln A}$, are given by inverting Eqs.(8) and (12) after making assumptions about the properties of hadronic interactions.

In Fig.5, the two lowest order moments of the logarithmic mass are shown as functions of primary energy [58]. They were obtained at the PAO from the FD measurements while using the three models of hadronic interactions that were either tuned to recently available LHC data, QGSJet II-04 [59] and Epos-LHC [60, 61], or found in good agreement with it, Sibyll 2.3 [62, 63]. One learns that the mass composition evolves from mixed to light primaries towards the ankle region ($E \approx 5$ EeV). With increasing energy above the ankle, the mass composition gets heavier while compatible, on average, with the nitrogen component. Furthermore, the sample variance of the logarithmic mass deduced with the help of Epos-LHC and Sibyll 2.3 models

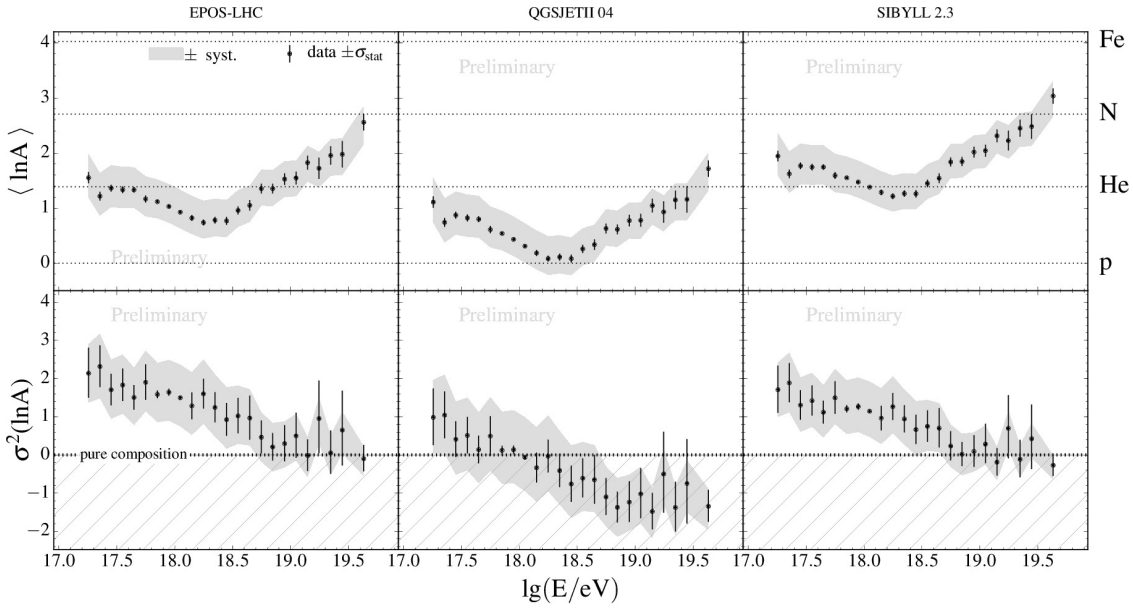

Figure 5: Average values of the logarithmic mass (upper panels) and its standard deviations (lower panels) are shown as functions of primary energy. They are estimated from the FD data collected at the PAO using Epos-LHC [60, 61] (left panel), QGSJet II-04 [59] (middle panel) and Sibyll 2.3 [62, 63] (right panel) interaction models. Reproduced from Ref. [58].

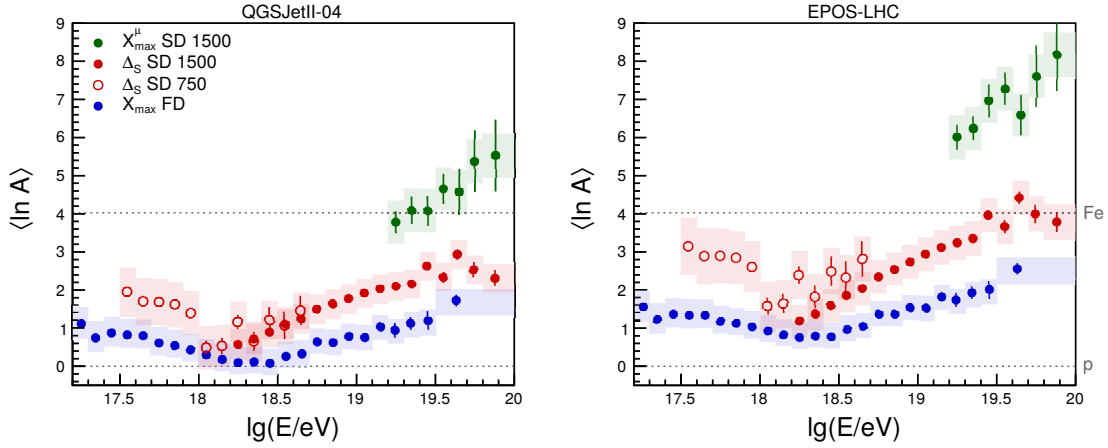

Figure 6: Energy evolution of the average logarithmic mass predicted by the QGSJet II-04 [59] (left panel) and Epos-LHC [60, 61] (right panel) models of hadronic interactions. The results from FD measurements of the depth of shower maximum (blue points) [39] are compared with the results based on estimates of the muon production depth (green points) [44] and with the rise time results (red point and circles) [46]. Reproduced from Ref. [64].

suggests that the primary beam of cosmic particles is composed of different nuclei at lower energies and is dominated by a single type of nucleus at the highest energies (lower left and right panels in Fig.5). However, unphysical negative standard deviations of the logarithmic mass are obtained above 1 EeV with the QGSJet II-04 model (lower middle panel in Fig.5).

The average values of the logarithmic mass deduced from the SD measurements [44, 46] are compared with those values obtained from the FD observables in Fig.6, when using the two models of hadronic interactions, QGSJet II-04 [59] and Epos-LHC [60, 61]. The weaknesses of the hadronic models are well visible, reflecting the fact that different EAS components, the electromagnetic and muonic component (see Sections 4.1.1 and 4.1.2), are considered in these analyses. Not only that neither of the two hadronic models can describe all three types of measurements at a time, but they also fail to describe the average production depths for shower muons unless trans-iron ($\langle \ln A \rangle > 4$) primaries are taken into account.

Let us add that the relationship between the average values and standard deviations of the logarithmic mass and its implications for the existing models of hadronic interactions were originally discussed in Ref. [65]. Furthermore, the relationship between the mass-related data recorded either by the FD telescopes or the SD stations (Section 3.4) showed that a mixed primary beam is preferred at the ankle region [66].

To sum up, the data collected at the PAO shows a clear structure in the energy evolution being confidently inconsistent with unchanged mass composition, all this notwithstanding the problems associated with hadronic physics at the highest energies. A thorough discussion of the $X_{\rm max}$ moments and the SD observables, including details about average values of the logarithmic mass and its standard deviations in the primary beam of cosmic particles, can be found, for example, in Refs. [3, 6, 39, 58]. The comparison of $X_{\rm max}$ results collected at the PAO to those of the Telescope Array experiment is summarized in Refs. [55, 56, 57], together with technical details of different methods used in data processing.

4.2.2 Mass components

In order to interpret the FD data in terms of mass fractions, the PAO presented several fits of the full $X_{\rm max}$ distributions using simulated templates for specific incident species [58, 67]. Regardless of non-negligible uncertainties in modeling of hadronic interactions, the goal was to maximize usable information from measurements, thereby reducing degeneracy of various composition mixtures when only the two lowest order $X_{\rm max}$ moments are taken into account. The best fit of fractions was obtained within a binned maximum-likelihood method that also provide information on the goodness of the fits.

Energy dependent mixtures of four primary masses (protons, and helium, nitrogen and iron nuclei) are shown in Fig.7. In this figure, the percentage of each primary is shown as a function of primary energy. Similar plots for two and three primary species can be found in Ref. [67]. Composition fractions were obtained by

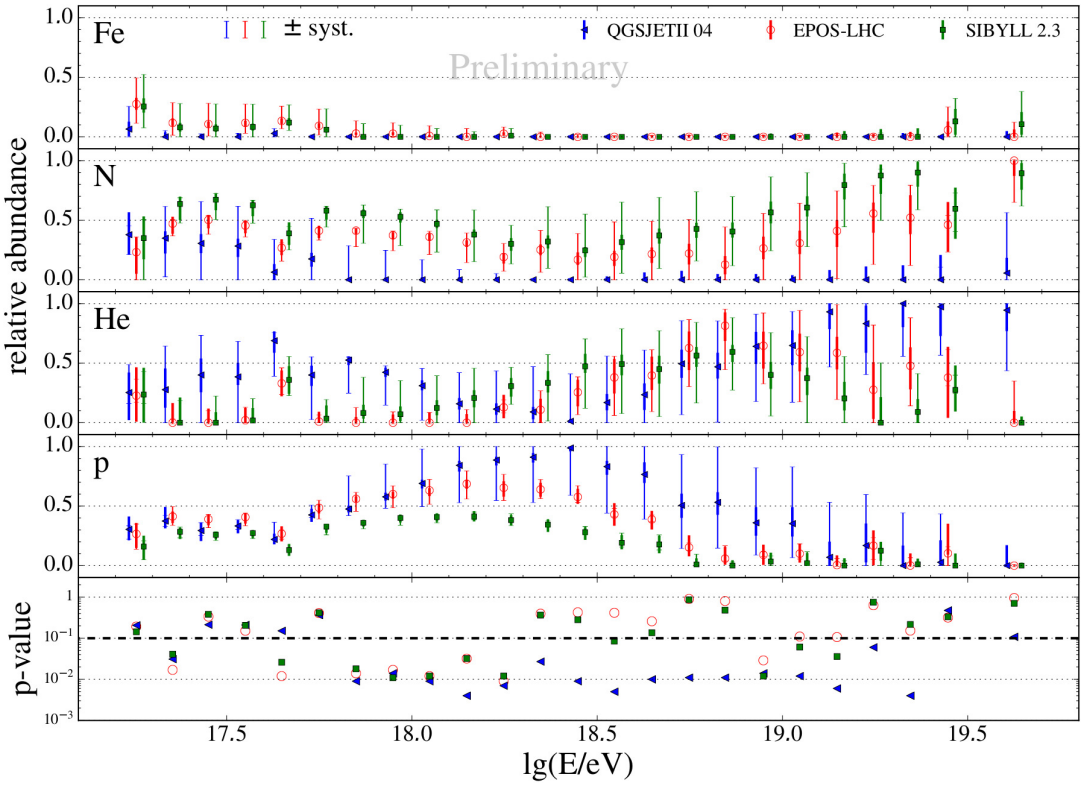

Figure 7: Fitted mass fractions and qualities for the scenario of complex mixtures of primary protons with nuclei of helium, nitrogen and iron, obtained with the Epos-LHC [60, 61] (red), QGSJet II-04 [59] (blue) and Sibyll 2.3 [63] (green) models of hadronic interactions. The four upper panels show the species fractions. Thick error bars denote the statistical uncertainties, thin error bars are for the systematic ones. The lower panel shows the p-values of corresponding fits. The horizontal dotted line in the lower panel indicates $p = 0.1$. Reproduced from Ref. [58].

interpreting the data with three models of hadronic interactions, as indicated.

The main results are as follows. Firstly, a similar behavior is predicted with a large fraction of protons at primary energies near below the ankle, around 2 EeV, where most FD data was collected at the PAO. Secondly, a sub-dominant iron component considered throughout the energy range is consistent with the measured $X_{\rm max}$ distributions, regardless of the models used. Thirdly, it turned out that, with the current models of hadronic interactions, acceptable fits of the $X_{\rm max}$ distributions (p-value > 0.1) can be obtained only when primaries of intermediate masses are included into the analysis. But the overall accuracy of the deduced fractions is not good. Finally, there are remarkable discrepancies between mass components obtained by using different models of hadronic interactions. This fact does not allow to draw a definitive conclusion about the mass composition in the primary beams of ultra-high energy cosmic rays [58, 67].

4.3 Dispersion of primary masses

A commentary on publication [A01].

In our simulation study [A01], we proposed a way of examining the variance of the logarithmic mass of primary cosmic rays, see Section 4.1.1. This analysis is linked to our interest in the understanding of different kinds of shower signals registered by the FD and SD [P25, P29, C11], with the emphasis placed on the estimate of muon content in the EAS [C06, C07, C12]. All these studies that aim to improve our knowledge of mass-related observables and simplify primary mass discrimination were thoroughly discussed at the Pierre Auger Collaboration, some of them were presented at conferences.

We considered a hypothetical observatory of UHECRs consisting of two complementary SD arrays collecting, respectively, the electromagnetic and muonic signals induced by extensive air showers. These signals were determined by the ground densities of corresponding particles registered at a specific distance from the shower core. The fact was used that the electromagnetic and muonic signals depend differently on the mass and zenith angle of incident particle, see Section 4.1.2. The muonic signals induced by different primaries are well differentiated by their size, see Eq.(15), while their zenith angle dependence is rather moderate. On the other hand, the electromagnetic signals drop sharply with increasing zenith angle, but only slightly depend on the type of incident particle, see Eqs.(16) and (17). It is worth mentioning that currently only the combination of these two types of signals is registered by the SD array at the PAO, see Section 3.4.

Typical features of EASs were simulated with the help of the two post-LHC models of hadronic interaction, QGSJet II-04 [59] and Epos-LHC [60, 61]. This way, we obtained detailed information on mass-dependent attenuation curves, which reflect dependencies of the electromagnetic and muonic signals on zenith angle (see Eqs.(15) and (16)). The shower characteristics, including signal fluctuations and correlations between signals, when smeared by detector imperfections, were utilized as inputs to simplified simulations of the two ground signals caused by EASs generated in a wide range of initial conditions (primary energy, mass and zenith angle).

We examined beams consisting of four types of primary species (protons, and helium, nitrogen and iron nuclei) and mixed in many different ways. For a given primary beam incident at a given zenith angle, two sets containing a chosen number of events with the highest electromagnetic or muonic signals, respectively, were compared with the aim to infer the relative number of matched events. It was demonstrated that the spread of primary masses increases with the parameter that represents the difference in the numbers of matched events between vertical (zenith angle $\theta = 0^\circ$) and slanted (we choose $\theta = 45^\circ$) showers. Corresponding correlation coefficients (typically around 0.90) were shown to be increased with increasing average value of the primary mass.

The robustness of the proposed method was examined in additional Monte Carlo

simulations. The studied relationship remains valid when the ground signals are derived from the number of secondary particles above differently chosen threshold energies even if these secondaries are collected in different distances from the shower core. Modeled less significant fluctuations and correlations of signals also leave our results almost unaffected. Moreover, the analysis conducted using the two post-LHC models indicates a weak dependence on the details of hadronic interactions.

In summary, we suggested a new type of SD measurement of the mass spread in UHECR beams with a view to obtaining information independent of the FD measurements (Section 4.2). This technique distinguishes between electromagnetic and muonic components of EASs and have a nearly 100% duty cycle. Such detection devices are now being built at the PAO [64] (Section 3.3). The SD stations will be equipped on top with a plastic scintillator. An integrated analysis of the water Cherenkov and scintillator signals will enable the counting of shower muons hitting the ground while isolating the electromagnetic component.

4.4 Maximum entropy composition

A commentary on publication [A02].

In our study [A02], we described a novel approach based on the principle of maximum entropy which solves the partition problem of the primary mass composition of UHECRs, while using the two lowest order $X_{\max}$ moments obtained from the FD measurements (Section 4.2). This method and its application was presented at a conference [C05]. It was also discussed within the Pierre Auger Collaboration. When applied to the real data collected at the PAO during the last ten years [39], we obtained results [P26, P27] that confirm presented trends of the primary mass composition (Section 4.2.2) [65, 67], see also the most recent analysis in Ref. [58].

Our motivation stems from the fact that currently available models of hadronic interactions provide remarkably different solutions to the composition problem and in some cases even indicate possible inconsistencies in the modeling of hadronic interactions [39, 58, 64, 65, 67], see Sections 4.2.1 and 4.2.2. The aim was to show what kind of information can be inferred with limited knowledge we have about processes underlying observations of EASs. In order to learn what trends in the primary composition are consistent with observations, we adopted the principle of maximum entropy [68, 69, 70, 71] supplemented with a simple model of shower development (Section 4.1.1). This approach provides the discrete probability distribution over a selected set of primary particles causing extensive air showers.

In this concept, we assumed that experimental information consists of energy dependent sets of the two lowest order central moments of the depth of shower maximum, $\langle X_{\max}\rangle(E)$ and $\sigma^2_{\max}(E)$, see also the introductory part of Section 4.2. In order to deduce occupancies of primary particles, we related these shower observables to mass moments of incident primaries using the shower model described in Section 4.1.1. In particular, we utilized Eqs.(8) and (12). The mean depth of

shower maximum for protons at a reference energy, $C = \langle X^{\rm p}_{\rm max}\rangle(E_0)$, see Eq.(8), and the elongation rate, $D = d\ln 10$, introduced in Eq.(6) were considered as unknown parameters, which depend on the properties of hadronic interactions. Parameters related to shower fluctuations, the mean variance of the depth of the first or main interaction and the mean variance of the depth connected with the subsequent shower development, $\langle\sigma^2_{\rm fr}\rangle$ and $\langle\sigma^2_{\rm sh}\rangle$, see Eqs.(10)-(12), were estimated based on the assumptions that are in line with our understanding of shower physics.

The partition problem was solved using two suitably chosen observation-based constraints treated on an equal footing in a setting that deliberately avoids assuming any other facts. Given the shower parameters (C and D, see Eqs.(6) and (8)), we proposed a way to gain a unique, well-behaved solution among various options of how to combine chosen primary components (mainly protons, and helium, nitrogen and iron nuclei). This was achieved by maximizing missing information so as to obtain the two lowest order $X_{\rm max}$ moments within a simple model of shower development described in Section 4.1.1.

To sum up, the main results are the following. We focused on showing how to treat the two lowest order $X_{\rm max}$ moments, and possibly other average observables, in order to assign the occupancy probabilities to particles in the primary CR beam causing extensive air showers, including the energy dependence. The proposed method and the interpretation of its results were summarized with the emphasis that this concept is quite distinct from and independent of other procedures used so far in composition studies. The method exploits partial knowledge of investigated phenomena and returns a maximally noncommittal distribution of the occupancy of primary particles that is constrained by information inferred from experiment, while relying on simple shower assumptions. Two representative data sets reminiscent of the current measurements (for the latest data see e.g. Refs. [8, 58]) were examined and the resulting outputs were discussed in detail. Given the set of primary species, it turned out that the shower parameters are limited through accessible solutions in the whole inspected energy range. This makes our treatment suitable for testing assumptions about hadronic interactions provided that the basic facts we have adopted for describing extensive air showers are correct.

5 Arrival directions

The existence of UHECRs has been know for more than 50 years but their sources and mechanisms of their production have not yet been identified. The shape of the energy spectrum in the EeV range (Section 5.2), supported by the data on the primary mass composition (Section 4.2), indicate that different types of sources are observed [5, 6]. The lack of fluxes of secondary photons [20] and neutrinos [21] at EeV energies rules out the possibility that the most energetic CRs originate from the decay or annihilation of super-heavy relic particles. This suggests that charged massive particles are accelerated by electromagnetic processes in special regions in the universe. Hence, the distribution of arrival directions of the highest energy cosmic particles (typically $E > 40$ EeV) is expected to provide the direct evidence on the location of accelerating objects.

Exploring the links between registered arrival directions of UHECRs and the positions of their sources is made difficult due to not fully knowing conditions during their propagation in intergalactic space, which is not transparent to them. The distance that CRs travel from their sources to a detector on Earth is limited by their energy losses through interactions with the photon fields, such as the cosmic microwave background (CMB) and the extragalactic background light (EBL), represented by infrared, optical and ultra-violet photons. The intervening magnetic fields in the extragalactic space and in the Galaxy cause deflections that modify arrival directions of CRs. Finally, the above-mentioned effects depend on the energy supplied to unknown types of CRs (Section 4) by unknown accelerating mechanisms.

This section deals with the topics related to searches for astrophysical point sources of the most energetic particles ($E > 40$ EeV) through their angular distribution measured at the PAO. The basic factors affecting cosmic particles during their propagation from sources to a detector on Earth are described in Section 5.1. Based on the current interpretation of CR data, the characteristics of possible extragalactic sources are mentioned. The related information on the measured CR flux is summarized in Section 5.2, showing how this flux is conditioned by UHECR production and propagation through radiation backgrounds. Directional results that have been discussed at the PAO during the past years are given in Section 5.3. The recent papers of the author and his co-worker [B01, B02] are introduced and commented in Section 5.4, and reprinted in Appendices C and D.

5.1 Propagation of cosmic rays

5.1.1 Energy losses

The most energetic cosmic particles lose energy by different ways when traveling through the space. All cosmic particles produced at cosmological distances lose energy adiabatically as the universe expands. This energy loss dominates for protons with energies up to 1 EeV and for nuclei with the mass number A and energies

typically $E < A$ EeV. The corresponding energy loss length[2] is $L = cH_0^{-1} \approx 4$ Gpc, where H_0 denotes the Hubble constant. At higher energies ($E > A$ EeV), the main energy loss mechanism is the production of e^+e^- pairs due to CMB photons. At very high energies, typically $E > 100\,A$ EeV, most relevant for directional studies, the energy losses are dominated by the photo-production processes that occur with an appreciable rate. Cosmic protons undergo photo-meson interactions on CMB photons. For nuclei at these energies, photo-disintegration processes occur on the CMB and EBL, in which a nucleus is stripped by one or more nucleons. These effects were recognized by K.Greisen [10], G.T.Zatsepin and V.A.Kuzmin [11] soon after the discovery of the CMB. These authors independently pointed out that the energy spectrum of cosmic particles would drop sharply at an energy range of 40-60 EeV, provided that CRs are produced with energies in excess of 100 EeV in sources spaced homogeneously throughout the universe (GZK effect).

A photo-production interaction is possible when the center of mass energy of the interaction, $\sqrt{s}$, is higher than the sum of masses of final particles. In a collision of a cosmic proton with a CMB photon of energy $\epsilon \approx \langle E_{\rm CMB} \rangle = \frac{\pi^4}{30\xi(3)} kT \approx 0.6$ meV, where $T = 2.73$ K is the temperature of the CMB photons, in processes

$$p + \gamma_{\rm CMB} \to p + \pi^0, \qquad\qquad p + \gamma_{\rm CMB} \to n + \pi^+, \tag{18}$$

it must hold $s \approx m_p^2 c^4 + 2E_p\epsilon(1 - \cos\phi) \geq (m_p + m_\pi)^2 c^4$, where m_p and m_π are proton and pion rest masses, respectively, E_p is a proton energy and ϕ denotes a collision angle in the system of observer. In a head on collision ($\phi = 0^\circ$), we estimate a typical threshold energy for the cosmic proton to be

$$E_p^{\rm th} \approx \frac{m_\pi c^2}{4\epsilon}(2m_p + m_\pi)c^2 \approx 100 \text{ EeV}. \tag{19}$$

Obviously, there are many CMB photons with higher energy (for example, the CMB energy density is about 1/10 of its maximum at 2 meV) and cosmic protons start to interact with them having lower energies, thus triggering the GZK effect.

Pion photo-production has been extensively studied on accelerators. In the center of mass system, the largest cross section is reached at the energy range of the rest energy of the Δ^+ resonance ($m_\Delta c^2 \approx 1232$ MeV, and $E_p^{\rm th} \approx \frac{(m_\Delta^2 - m_p^2)c^4}{4\epsilon} \approx 250$ EeV for head on collisions of cosmic protons with CMB photons of the mean energy), where the cross section is about 500 μb. After the resonance rest energy, the cross section decreases with increasing energy to 100 μb and then grows logarithmically. The mean interaction path of the cosmic proton in the CMB field is typically $\lambda = (n_{\rm CMB}\sigma_{p\gamma})^{-1} \approx 4$ Mpc for the photon density $n_{\rm CMB} \approx 400$ cm^{-2} assuming the interaction cross section $\sigma_{p\gamma} \approx 200$ μb. At the energy range of the Δ^+ resonance, the cosmic proton loses typically 20% of its energy (about $\frac{m_\pi}{m_p + m_\pi} \approx 0.13$ at the threshold energy). Hence, the proton energy loss length is less than five times

[2]The energy loss length, $L = -\left(\frac{1}{E}\frac{{\rm d}E}{{\rm d}x}\right)^{-1}$, is the distance along which a particle loses $1/e$ of its initial energy. Based on averaging, it is used when the propagation path far exceeds the mean free path.

longer than its mean interaction path, $L \approx \frac{E}{\Delta E}\lambda \leq 20$ Mpc corresponding to a proton flight time of about 60 My, and it decreases with increasing energy.

Realistic estimates of energy losses are shown in Fig.8. For example, it is documented how the mean free path for cosmic protons in the CMB field steeply decreases with increasing energy above 50 EeV and achieves a value of about 10 Mpc in the 100 EeV range. Thus, a cosmic proton registered with an energy of 60 EeV has only about 50% chance that it has not interact with the CMB when having come from beyond 100 Mpc [72]. In a similar way, cosmic protons registered with energy above 100 EeV have only less than a 0.1% chance of having traveled more than 100 Mpc through the CMB [72]. Based on the pion photo-production, the GZK horizon[3] for cosmic protons with energies above 60 EeV is typically 200 Mpc [73].

The composition data indicate (Section 4.2) [39, 58, 67] that also nuclei with extreme energies can escape from an acceleration region, and then these nuclei or their products can be recorded by a detector on Earth. In such a case, both CMB and EBL play the important role. When traveling through the CMB, cosmic nuclei lose most energy in photo-disintegration processes [10, 11] by stripping one or more nucleons, for example, in reactions (γ, n) and (γ, p), when

$$A + \gamma_{\rm CMB} \rightarrow (A - kN) + kN, \tag{20}$$

where A is the mass number of a nucleus, N denotes the nucleon and k stands for the number of stripped nucleons. The threshold energy of this process is not far from the threshold energy for the pion photo-production induced by protons on the CMB. For a head on collision of a heavy nucleus with a CMB photon of energy $\epsilon \approx \langle E_{\rm CMB} \rangle$, one gets for one chipped nucleon from the parent nucleus, formally,

$$E_A^{\rm th} \approx \frac{(m_{A-1} + m_N)^2 c^4 - m_A^2 c^4}{2\epsilon} \approx \frac{m_A c^2 S_N}{2\epsilon} \approx 5\ A\ {\rm EeV}, \tag{21}$$

where $m_A c^2 \approx A$ GeV and $S_N \approx 6$ MeV is a typical value of the separation energy of the nucleon. For iron nuclei, the threshold energy is in the 100 EeV range, see Fig.8.

At this energy range, the mean free path for iron nuclei in the CMB field is shorter than 1 Mpc. The key intermediate state is now the giant dipole resonance (typically $E_{\rm D} \approx$ 10-20 MeV and $E_A^{\rm th} \approx \frac{m_A c^2 E_{\rm D}}{2\epsilon} \approx 10\ A$ EeV for head on collisions with CMB photons of the mean energy). The threshold energy and the mean free path are reduced accordingly for nuclei with intermediate masses [5, 15].

Detailed calculations [15], including information on cross sections, indicate that only iron nuclei behave similarly to protons when propagating through the space [5]. Lighter nuclei, like helium or CNO nuclei, lose energy faster. Typically, about 10% of helium nuclei (CNO nuclei) with energies in excess of 60 EeV can reach the Earth from the distance larger than 10 Mpc (30 Mpc) [5, 73], while the horizon for iron nuclei is only slightly smaller than the GZK horizon for protons (about 200 Mpc for

[3]The CR horizon at a given energy is taken to be the distance from which originate 90% of the registered CR particles having higher energies. For cosmic protons, this distance is referred to as the GZK horizon.

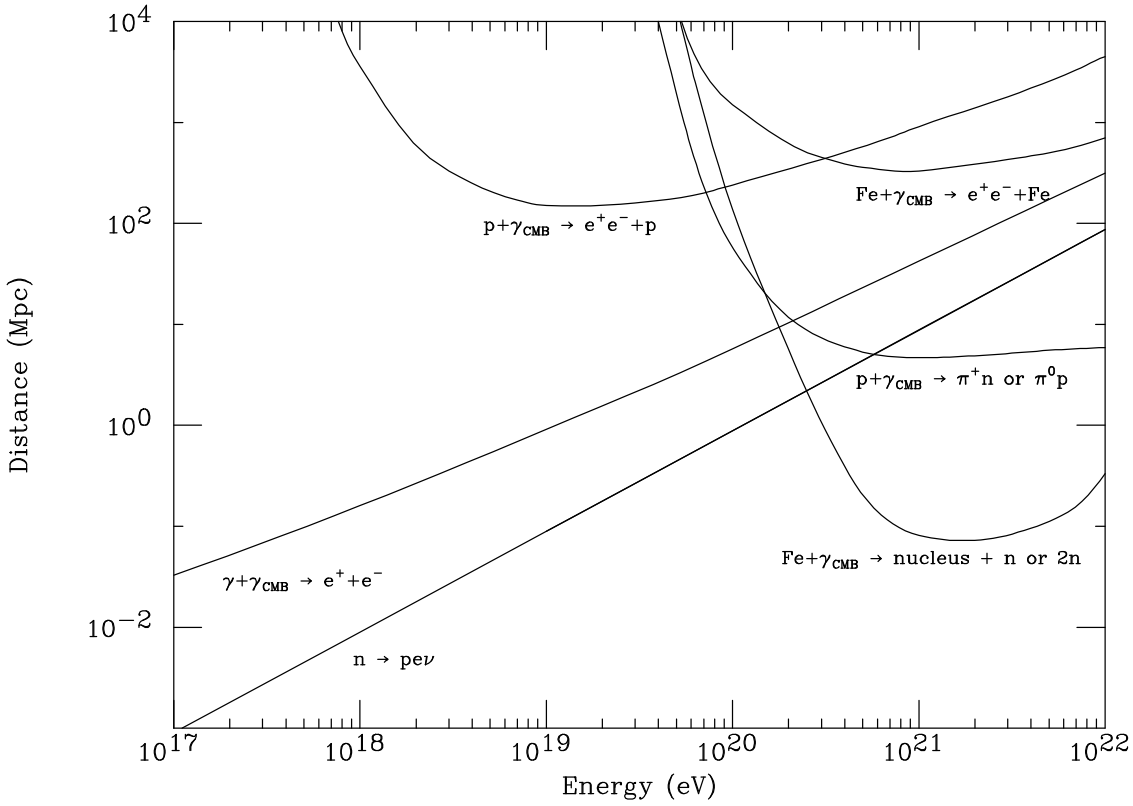

Figure 8: Interactions of possible cosmic particles with CMB photons. The curves marked by $p + \gamma_{\rm CMB} \to e^+e^- + p$ and $\mathrm{Fe} + \gamma_{\rm CMB} \to e^+e^- + \mathrm{Fe}$ are energy loss lengths due to pair production. The curve marked by $p + \gamma_{\rm CMB} \to \pi^+ n$ or $\pi^0 p$ is the mean free path for photo-pion production of a proton. The curve indicated by $\mathrm{Fe} + \gamma_{\rm CMB} \to$ nucleus $+ n$ or $2n$ is the mean free path for a photo-nuclear reaction in which one or two nucleons are removed off the nucleus. The curve marked $\gamma + \gamma_{\rm CMB} \to e^+e^-$ is the mean free path for the interaction of a high-energy photon and added is the mean decay length for a neutron indicated by $n \to pe\nu$. Taken from Ref. [72].

$E > 60$ EeV) [5]. These disparities suggest that a very complex mixture of species may arrive at Earth, with the composition depending on what particles and with what energy were produced in the sources and upon the paths along which these particles or their daughter products having traveled through the radiation fields.

Cosmic protons and nuclei also lose energy by pair production. When a cosmic nucleus of a rest energy $m_A c^2 \approx A$ GeV, where $A \geq 1$ is the mass number, interacts with the CMB, producing the e^+e^- pair in a process

$$A + \gamma_{\rm CMB} \to A + e^+ + e^-, \tag{22}$$

we get a typical threshold at somewhat lower energy

$$E_A^{\rm th} \approx \frac{m_e c^2}{\epsilon}(m_A + m_e)c^2 \approx A \text{ EeV}. \tag{23}$$

The pair production on the CMB takes place for cosmic protons of energies above 1 EeV. When producing the e^+e^- pair, the proton loses about $\frac{2m_e}{m_p} \approx 10^{-3}$ of its initial energy. The cross section of this process is much larger than the cross section for pion photo-production. Consequently, the proton energy loss is much smaller when compared to the pion channel but it is nearly continues.

The energy loss length for cosmic particles creating e^+e^- pairs in the CMB field always exceeds 100 Mpc, see Fig.8. Its minimum value moves from about 10 EeV well above 100 EeV with increasing particle mass, from cosmic protons up to iron nuclei. It is worth noting that the e^+e^- production induced by beams of cosmic protons on the CMB was interpreted as responsible for the dip or ankle observed at the upper end of the CR energy spectrum around 5 EeV (Section 5.2) [12, 13].

In summary, foreground sources should mainly contribute to the observed CR flux at the highest energies. Indeed, the CR horizon in the radiation fields is reduced with increasing CR energy, thus suppressing the flux contributions of remote emitters, from which only protons or nuclei, and possibly products of their disintegration, with degraded energies can be observed. This calls for considering both the spectral and compositional features when point sources of UHECRs are explored.

5.1.2 Magnetic fields

The interpretation of CR data in terms of anisotropy depends critically on the structure and strength of intervening magnetic fields. Simply expressed, a charged cosmic nucleus undergoes an angular deflection $\Delta\phi \propto \frac{ZeB_\perp}{E}$ that is directly proportional to its atomic number, Z, the strength of the magnetic field perpendicular to the direction of its propagation, $B_\perp$, and inversely proportional to its energy, E.

According to recent models of the Galactic magnetic field (GMF), the angular deflection of cosmic particles is a few degrees for rigidities $E/Z > 100$ EeV and can exceed tens of degrees in the $E/Z \approx 10$ EeV rigidity range [74]. For lower rigidity, $E/Z < 1$ EeV, CRs are assumed to diffuse in turbulent components of the GMF. In a similar way, CRs are also deflected and may longer propagate diffusively through intergalactic space in less intensive magnetic fields, which structures are far less known.[4] But, on the other hand, it is not excluded that strong magnetic fields of astrophysical objects can focus cosmic particles in a certain direction.

Regardless of details of how magnetic fields affect particle trajectories from their sources to a detector on Earth, the anisotropy in the distribution of arrival directions of extremely energetic CRs ($E > 40$ EeV) is expected to be observed in the case of a dominant source or for a very anisotropic angular distribution of sources, for example. In accord with the energy and mass dependence of UHECR propagation (Section 5.1.1), it is plausible to assume that the observed pattern of arrival directions will be related to the division of the nearby matter in the universe.

[4]Based on these considerations, a magnetic horizon is defined as a distance from which extragalactic CRs of a given energy propagate nearly rectilinearly to a detector on Earth, in a non-diffusive way.

5.1.3 Possible sources

The minimum requirement for the acceleration of charged cosmic particles is their containment at the site where they gain energy gradually. The condition on potential acceleration sites relates the maximum achievable energy $E_{\max}$ of a particle of a charge number Z with the linear dimension, R, and the strength of the magnetic field, B, of an accelerating object. Such a requirement is written as [75]

$$E_{\max} = 10\beta Z \left(\frac{B}{1\ \mu\mathrm{T}}\right)\left(\frac{R}{1\ \mathrm{pc}}\right)\ \mathrm{EeV}, \tag{24}$$

where β gives the characteristic velocity of the scattering centers or of the accelerating shock wave that supply energy to cosmic particles [75].

In assessing possible acceleration sites, the condition given in Eq.(24), along with sufficient luminosity and not too long distance (Sections 5.1.1 and 5.1.2), applies to different astrophysical objects, for more details see e.g. Ref. [2]. Among the possible candidates are neutron stars and other similar objects with strong magnetic fields. In such cases, direct acceleration is assumed to take place in an electric field induced at the surface. Other regions where the condition for the particle acceleration over 100 EeV is satisfied ($BR > 10^{-5}$ T·pc) are the cores and jets of active galactic nuclei, radio galaxies, merging galaxies or clusters of galaxies spread over a larger volume [2]. But also other scenarios are possible such as impulsive processes associated with gamma-ray bursts. The issues that are discussed in these scenarios include energy losses of accelerated particles due to synchrotron radiation, Compton processes, and interactions with the material surrounding sources [2]. Finally, it is worth noting that cosmic rays may originate from sources that have a limited time of life and cannot be currently identified.

Problems with the acceleration of CRs to very high energy can be circumvented by the idea that they are formed in the decay or annihilation of super-heavy relic particles. Such processes would produce quarks and leptons, and subsequent cascades of very energetic photons, neutrinos and a small portion of baryons. However, the latest experimental results from the PAO do not support such models [20, 21].

5.2 Remarks on the energy spectrum

The distribution of arrival directions of CRs is primarily sensitive to the population of their sources. Besides specific source conditions, the directional data is also affected by the interactions of charged cosmic particles with background fields. Along with the mass composition outcome (Section 4.2), the related propagation effects limit the distance of possible sources and modify particle trajectories (Section 5.1). These effects combined with source characteristics are reflected in typical features observed at the upper end of the CR energy spectrum, thus providing complementary evidence for the same reality. In the following, several arguments related to the directional analysis of the most energetic particles are mentioned.

The energy spectrum of CRs measured at the PAO spans almost over three orders of magnitude in energy [7, 76, 77]. The differential CR flux multiplied by the cube of energy is shown in the left panel in Fig.9. The spectrum from the main SD array starts at 3 EeV, including data from January 2004 to December 2016, with a total exposure 51588 km^2·sr·yr. The hybrid spectrum, when both FD and SD detectors are utilized, begins at an energy of 1 EeV. The low-energy branch of the spectrum, over 0.3 EeV, is obtained using the Infill array. In addition, the energy spectrum inferred with the help of inclined showers (zenith $60^\circ < \theta \leq 80^\circ$) starts at 5 EeV.

A combined energy spectrum [7] (accumulating about 67000 km^2·sr·yr of exposure) obtained by means of a statistical fit is shown in the right panel in Fig.9. This spectrum is described by [7]

$$J(E) = J_0 \left(\frac{E}{E_a}\right)^{-\gamma_1}, \qquad E \leq E_a, \tag{25}$$

$$J(E) = J_0 \left(\frac{E}{E_a}\right)^{-\gamma_2} \left[1 + \left(\frac{E_a}{E}\right)^{\Delta\gamma}\right] \left[1 + \left(\frac{E}{E_s}\right)^{\Delta\gamma}\right]^{-1}, \qquad E > E_a, \tag{26}$$

where J_0 is a normalization constant, $\gamma_1 \approx 3.29$ and $\gamma_2 \approx 2.53$ are measured spectral indexes below and above the ankle. As indicated in Fig.9, the hardening of the flux of cosmic particles at the ankle region is seen at $E_a \approx 5$ EeV. The suppression of the flux is observed at an energy of $E_s \approx 39$ EeV with a softening of $\Delta\gamma \approx 2.5$ towards ultra-high energies. The detection of several CRs with higher energies excludes the possibility that cosmic particles are mainly from extremely distant sources.

The energy at which the integral PAO spectrum above the ankle drops by a factor of two below what would be expected with no suppression is $E_{1/2} \approx 23$ EeV (see Fig.9) [7]. This result disagrees with the GZK scenario (Section 5.1.1), in which cosmic protons lose their energy in interactions with CMB photons during propagation to a detector, when $E_{1/2}^{\rm GZK} \approx 53$ EeV [13, 64]. Hence, probably a limited power of CR sources is observed in the PAO data.

From the experimental point of view, the situation is still unclear, however. Recently, the Telescope Array has reported that the energy spectrum of cosmic particles measured in the northern hemisphere is consistent with the GZK scenario [8, 9]. The GZK break was identified somewhat higher in energy, $E_s^{\rm TA} \approx 65$ EeV. In addition to the ankle or dip observed in the EeV range, the Telescope Array measured a less sharp suppression of the CR flux than it is observed at the PAO. In the GZK energy range, where anisotropies are expected, this disagreement cannot be reconciled with a constant energy shift without destroying the agreement at the ankle. In this respect, the most divergent outcome is in the observation of different regions of the sky and, connected with this, in the interpretation of the mass composition. The elongation rate data measured at the PAO [39, 58] suggests a transition from light to heavier primaries at energies near and above the ankle region (Section 4.2) [58, 67], whilst the Telescope Array results [78, 79] rather indicate light primaries. But also

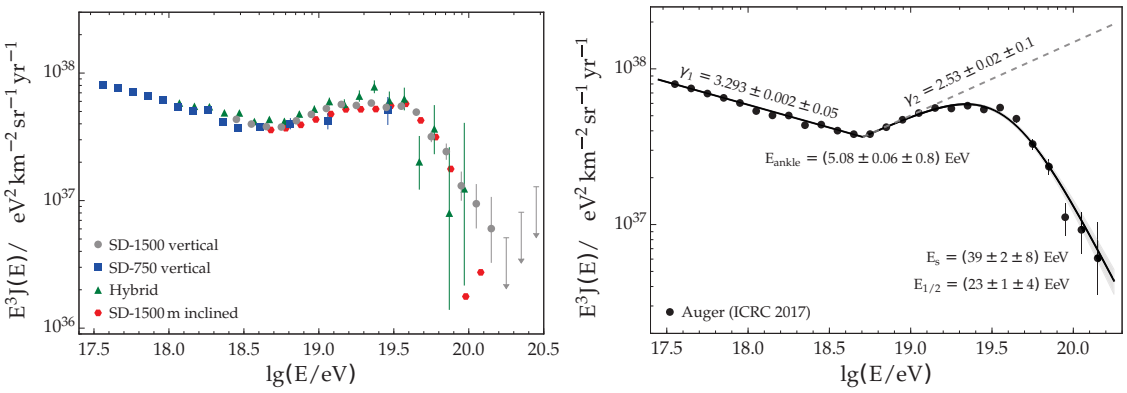

Figure 9: Energy spectrum of cosmic rays measured at the PAO. The observed differential fluxes multiplied by the cube of energy are depicted. The energy spectra measured by the SD array (SD 1500 m vertical, black points), the Infill array (SD 750 m vertical, blue squares), the hybrid detector (Hybrid, green triangles) and the energy spectrum of inclined showers for zenith angles $60° < \theta \leq 80°$ (SD 1500 m inclined, red circles) are shown in the left panel. The combined energy spectrum is depicted in the right panel. Taken from Ref. [7].

different experimental effects and processing methods can be responsible for this inconsistency. For the detailed discussion of these and related discrepancies between data collected by different experiments see e.g. Refs. [80, 81, 82].

In general, the variations of the spectral index at the highest energies should reflect the way of CR production and propagation. The final interpretation inevitably consists in a combination of spectral features with compositional and directional characteristics. Nowadays, there is no compelling observation-based explanation concerning the origin of the most energetic CRs, but several hypotheses do exist.

For example, if protons are observed at the upper end of the energy spectrum, as consistent with the data collected by the Telescope Array experiment [78, 79], the flattening around the ankle may be linked to the interaction of protons with the CMB and explained in terms of the pair production dip (Section 5.1.1) [13, 14]. Then the sharp decline in the CR flux corresponds to the GZK effect [10, 11].

However, if heavier nuclei dominate the upper end of the energy spectrum, as measured by the PAO experiment (Section 4.2) [39, 58], the situation is different [83]. The spectral shape of the CR flux accompanied by the increase of primary masses with rising primary energy can be explained by the transition from Galactic to extragalactic CRs below the ankle [84] and by the rigidity-dependent acceleration mechanism above it.[5] The ankle corresponds to the limited power of extragalactic accelerators for light small charged primaries while heavier species prevail at the highest energies [14, 15, 16]. It follows that the GZK effect for protons in the CMB applies weakly and, consistently with the PAO data [20, 21], the photo-production of

[5] A rigidity-dependent mechanism assumes that the maximum attainable energy of an accelerated nucleus scales with its charge Z, i.e. $E_{\max}(A, Z) = ZE^p_{\max}$, where $E^p_{\max}$ is the maximum energy for protons.

pions is reduced as well as the amount of photons and neutrinos from their decays. Unlike protons, arrival directions of cosmic nuclei are considerably deviated from the positions of their sources.

In another scenario, radiation fields surrounding CR sources are able to provide low-mass small charged components with steep energy spectra through photo-disintegration of heavy nuclei accelerated in sources [85], possibly in gamma-ray bursts [86]. Spallated nucleons account for the ankle feature. The CR flux suppression, heavier composition towards highest energies (Section 4.2) and greater deviations of arrival directions from source positions are dictated by the accelerator mechanism and by the propagation to Earth, while the GZK effect is largely avoided.

Let us add that the first attempt of the PAO to combine information about the spectral shape and mass composition of CR primaries measured above the ankle with plausible prepositions about their sources and propagation has been presented in Ref. [87]. This analysis suggests low maximum injection energy, hard energy spectra and heavy primary composition for homogeneously distributed CR sources.

5.3 The status of observations

The maximum distance of sources from which extragalactic UHECRs can arrive at Earth progressively decreases as their energy increases. This is a consequence of the energy losses due to pair production and pion photo-production by interactions of cosmic protons with CMB photons. Similarly, the loss processes in the CMB and EBL fields trigger a decrease of energy for cosmic nuclei and possibly lead to their disintegration (Section 5.1.1). With increasing CR energies and decreasing distance to their sources, the impact of extragalactic magnetic fields on their arrival directions is diminished (Section 5.1.2). Hence, the overall contribution of nearby sources becomes more important, leading to a larger expected anisotropy at the highest energies. Conversely, a lack of anisotropy, especially for protons, might further refine our knowledge of the CR production and propagation. These tasks require precise observation of the entire sky since the distribution of nearby sources is certainly not identical in different directions. Unfortunately, the existing inconsistencies in the interpretation of data collected by experiments operating in the southern and northern hemispheres (Section 5.2) have not yet allowed for a successful analysis.

Using the exceptional capabilities of the PAO various searches for CR sources were carried out by testing different anisotropic hypotheses. For this purpose, typically 50 events with energies in excess of 40 EeV registered in each year of observation were utilized. Among other studies, nearby objects taken from different astrophysical catalogs were examined whether they can be associated with recorded arrival directions of the highest energy events [22, 23, 24, 25], while preferring their extragalactic origin [26, 27]. Particular attention was paid to the nearest radio galaxies with active galactic nuclei, Centaurus A and Messier 87 [24, 25]. In the following, several representative analyses are described and their relevance is discussed.

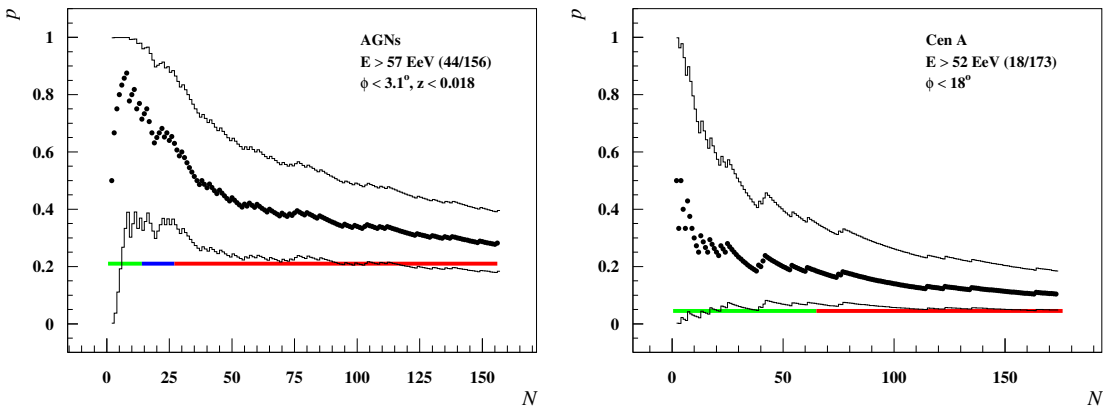

Figure 10: Left: Fraction of AGN events ($E > 57$ EeV, $\theta \leq 60°$) is plotted with black dots as a function of the total number of time-ordered PAO events recorded from 2004, January 1 to 2014, March 31 [25]. A 3σ (99.7%) confidence band around the most likely values is visualized by black broken lines. The horizontal line shows the isotropic value $p_{\rm iso} = 0.21$. Its green, blue and red sections indicate the first survey period, the second confirmation period and the following analysis, respectively. Right: Fraction of Cen A events ($E > 52$ EeV, $\theta \leq 60°$) from the same observation period with a 3σ confidence band are shown as functions of the total number of time-ordered PAO events. The horizontal line shows the isotropic value $p_{\rm iso} = 0.045$. The green line indicates the searching period, the red one is for the follow-up analysis.

5.3.1 Searches for point sources

The excellent performance of the PAO detector has opened the prospect of searching for point sources very soon after it started operating. After collecting a SD exposure of 4390 km^2·sr·yr, it was noticed that arrival directions of the most energetic events point close to positions of active galactic nuclei (AGNs) summarized in the Véron-Cety and Véron (VCV) catalog [88]. A detailed analysis, including a prescribed test, confirmed that most of the arrival directions of registered events (12 out of 15) with energies above 57 EeV appear closer than 3.1° from the positions of AGNs not distant more than 75 Mpc (redshift $z < 0.018$). The analysis was repeated when the SD exposure more than doubled (8890 km^2·sr·yr), the total number of events reached 27, and 17 of them (63%) were found to be associated with AGNs while only 5.7 events were expected (21%) for the isotropic distribution of sources [22, 23]. The analysis was updated in 2010 after the SD exposure of 20370 km^2·sr·yr was achieved. The signal weakened since only 29 out of 69 events (42%) were found to be associated with the chosen set of AGNs [24]. The latest update presented in 2015 states that 49 AGN events out of 160 events (31%) were observed above 52 EeV when the SD exposure grew up to 51753 km^2·sr·yr and both vertical (zenith angle $\theta \leq 60°$) as well as incline ($60° < \theta \leq 80°$) showers were included [25]. The signal development is shown in the left panel in Fig.10. It comprises only vertical showers ($\theta \leq 60°$) collected from 2004, January 1 up to 2014, March 31 [25].

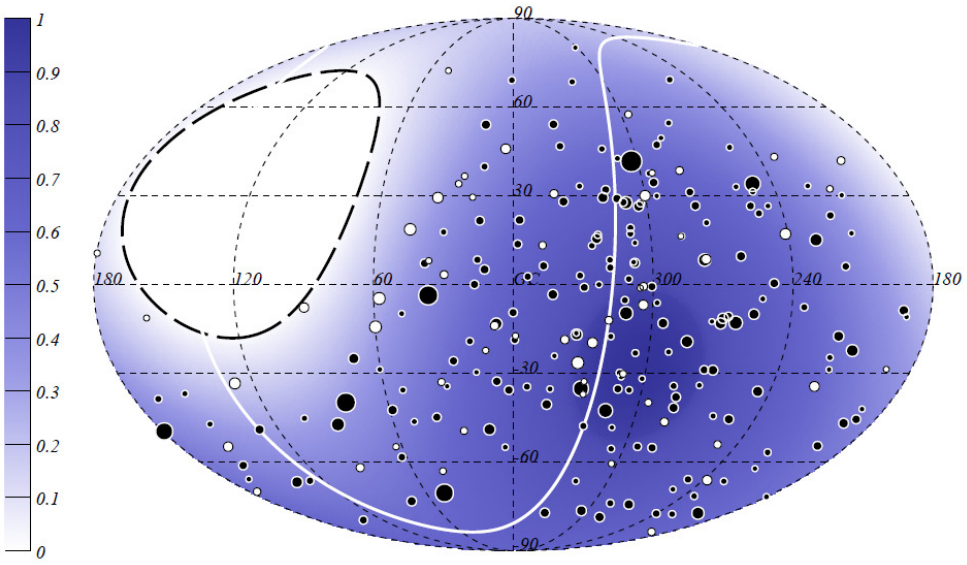

Figure 11: Map in Galactic coordinates of arrival directions of 231 PAO events with energies above 52 EeV. The dark filled circles correspond to 176 events in the vertical sample ($\theta \leq 60°$). The white filled circles correspond to 55 events in the inclined sample ($60° < \theta \leq 80°$). The size of the circles scales with the energy of events. The background blue color in the map indicates the relative exposure of the PAO to different declinations. The white region is outside the field of view of the PAO. Centaurus A is located at $(l, b) \approx (310°, 19°)$. Taken from Ref. [25].

In the AGN analysis [22, 23, 24, 25] only the anisotropy of CRs as such was emphasized. The reason was that the actual sources cannot be directly identified within the tested set of nearby AGNs. In fact, the AGN analysis does no distinguish between strong and weak emitters nor does it take account of their distances. The set of AGNs includes many low power objects that can hardly accelerate particles to the highest energies. The GZK horizon for protons with energies above 60 EeV, about 200 Mpc (Section 5.1.1), is much larger than the limiting distance in the AGN model, i.e. $D < 75$ Mpc ($z < 0.018$) [22, 23]. Hence, in summary, the result of the whole analysis is only the finding that the arrival directions of CRs recorded by the SD at the PAO are not spread isotropically on the sky. In Fig.11, the current set of the PAO arrival directions with energies above 52 EeV is shown [25]. Both vertical (zenith angle $\theta \leq 60°$) as well as inclined ($60° < \theta \leq 80°$) events are depicted.

The arrival directions of the highest energy CRs registered at the PAO were further examined adopting different plausible scenarios and using new analysis techniques. The main focus was on linking recorded arrival directions with objects summarized in various surveys or with known structures in the universe. Firstly, several tests were presented that aimed to search for signals of anisotropies relying upon the nearby structure. No significant excesses of the highest energy events were found around the Galactic Center [25, 89] nor in the vicinity of the galactic

plane [25], suggesting that CR sources are unlikely to be Galactic. It was also found that a non-negligible fraction of the CR flux arises from extragalactic objects situated not very close to the supergalactic plane [25]. Secondly, considering that the CR luminosity is proportional to the flux in the respective wavelength for the studied objects, by weighting for these fluxes, the distribution of detected arrival directions was compared with the positions of different populations of nearby galaxies. The 2MASS Redshift Survey, AGNs detected in X-rays by Swift-BAT and nearby radio galaxies with jets were examined [24, 25]. But all these possible associations were found not to be well constrained with the present data collected at the PAO.

Recently, promising analyses have been motivated by observations of γ-ray spectra collected by the *Fermi*-LAT from 17 bright nearby AGNs (γAGNs) and 23 nearby starburts galaxies (SBGs) [90, 91]. The anisotropy pattern of CR arrival directions gathered by the PAO detector was shown to be favored for both source models considered, but also other types of sources contribute. These results were obtained by optimizing an excess fraction and angular scale of the observed clustering around the positions of either γAGNs or SBGs. The numbers of events pointing in the vicinity of tested sources were modified by observed γ-ray fluxes, as suggested by the propagation features and by the presence of intervening magnetic fields (Section 5.1).

To summarize, no discrete source nor a simple enough structure of similar sources has yet been identified unambiguously based on several hundreds of PAO events with extreme energies ($E > 40$ EeV). All these and many supporting analyses indicate that there are multiple astrophysical models that may describe satisfactorily the observed set of arrival directions relying on the distribution of matter in the nearby universe. This feature can be explained in a scenario in which the number of individual sources contributing to the UHECR flux is large. Alternatively, these results could also be understood as due to large deflections caused by intervening magnetic fields (Section 5.1.2) provided a large amount of primary UHECRs in this energy range are heavy, as suggested by mass composition studies (Sections 4.2 and 5.2) [39, 58, 67], while their source distribution need not to be isotropic.

5.3.2 Centaurus A

Centaurus A (Cen A) is the nearest radio-loud active galaxy, situated at a distance of 3-4 Mpc at right ascension and declination $(\alpha, \delta) \approx (201^\circ, -43^\circ)$. Moreover, a large concentration of galaxies, the nearby Centaurus cluster, lies in approximately the same direction at a distance of about 50 Mpc. Therefore, the Cen A zone is an obvious candidate for searching sources of extremely energetic CRs on the southern sky. The region around Cen A was extensively examined from the beginning of SD observations at the PAO. The time evolution of the originally defined Cen A signal (events with energies $E > 52$ EeV and arrival directions pointing to a 18° radius circle [P02]) is documented in the right panel in Fig.10.

The excess of arrival directions in the vicinity of Cen A is easily recognized in a thorough energy-dependent search for overdense circular regions all over the sky [24].

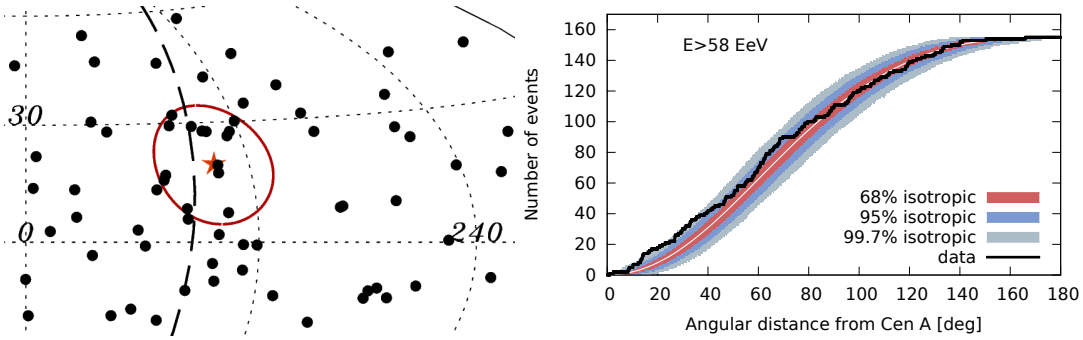

Figure 12: Left: Map in Galactic coordinates of the region around Cen A, showing arrival directions of PAO events with energies $E \geq 58$ EeV (black dots) and a red circle of a 15° radius around the direction of Cen A, indicated by a star, $(l, b) \approx (310°, 19°)$. Vertical (zenith $\theta \leq 60°$) as well as inclined ($60° < \theta \leq 80°$) events are included. The dashed line indicates the supergalactic plane. Right: The cumulative number of events in the Cen A region for the minimum energy of $E_{\rm min} = 58$ EeV, exploring the whole angular range. The 68%, 95% and 99.7% ranges corresponding to isotropy are indicated by colored bands. Taken from Ref. [25].

Currently, the largest signal is observed in a 15° radius circle centered in the position of Cen A for vertical (zenith angle $\theta \leq 60°$) and inclined ($60° < \theta \leq 80°$) events with energies above 58 EeV [25]. In this circle, there are 14 events out of a total of 155 events collected while 4.5 ones are expected on average from the isotropic distribution. Moreover, two arrival directions point very close to the position of the Cen A nucleus, see the left panel in Fig.12. Aside from those two events, the excess is distributed rather broadly in the whole region along the supergalactic plane, which is densely populated with different types of nearby extragalactic objects. In fact, the UHECRs with arrival directions pointing to the vicinity of the Cen A region make a strong contribution when associations with different populations of nearby extragalactic objects are studied [22, 23, 24, 25, 90, 91].

The observation of the region around Cen A and the Centaurus cluster offers an interesting comparison with the radio galaxy Messier 87 (M87), the second brightest galaxy located in the center of the northern Virgo Cluster [24]. In the vertical data collected up to 2014, March 31 [25], 17 out of 163 extremely energetic events ($E > 52$ EeV) were observed from the Cen A direction in a circle with a radius of about 18° while about 7.3 events from isotropic background are expected. In the vicinity of M87, where 2.4 background events are estimated, only 2 such events were found in a circle of the same radius [25]. However, the northern declination of the M87 radio galaxy (about three times less exposure when compared to the Cen A zone of an equal size) and distance (about 16 Mpc versus 3-4 Mpc for Cen A) result in about 50 times less events from the M87 region than from the Cen A zone provided that the Cen A and M87 radio galaxies are equally luminous in CRs. On the other hand, since the Centaurus Cluster of galaxies is about three times more distant than

the Virgo Cluster composed of a number of bright galaxies (about 52 Mpc versus 16 Mpc for the Virgo Cluster), events from the Virgo Cluster should outnumber those from the Centaurus Cluster by about 3 : 1 if the two clusters have equal CR luminosities. When confronted with the PAO data, the latter option is unlikely even though it is assumed that possible sources in the Virgo Cluster are much weaker.

The properties of the Cen A signal (angular, energy and time distributions of events) reflect our current knowledge of topics (composition, propagation) relevant for exploring the origin of extremely energetic CRs. This suggests that the follow-up Cen A data should have the capacity to provide specific insight into these issues. The simplest resolution would be through the identification of a large fraction of heavy nuclei in UHECR beams. Such a scenario would admit the high degree of isotropy observed on the southern sky, thus allowing to explain the blurred signal from the Cen A zone as well as the difficulty in searching for other potential CR sources. It would also ease acceleration problems and agree with the main features at the upper end of the energy spectrum (Section 5.2). In addition, this solution could also provide a scope for clarifying some inconsistencies that occur when comparing the fluorescence and ground-based signals induced by EASs (Section 4.2). At present, however, we have only limited information on the primary mass composition above 10 EeV (Section 4.2) [58, 78, 79] that is insufficient to verify this option.

5.4 Analysis of directional data

A commentary on publications [B01] and [B02].

In our studies [B01, B02], we focused on how to evaluate the presence of a weak source of events masked by background. We dealt with an on-off experiment designed for counting two classes of events, source and background events, the type of which cannot be distinguished in principle. The problem of assessment of a possible source of events was addressed from a Bayesian point of view. Our intention was to provide different insights pertaining to the on-off problem that benefit from their simplicity and naturally allow for the inclusion of additional data into the analysis.

We were primarily motivated by the fact that various analyses have not yet been able to unambiguously detect anisotropies in arrival directions of CRs that could limit the processes involved in their production. The possibility that such a goal could be achieved in the near future is also challenged by a new finding that the CRs become heavier at the highest energies (Sections 4.2 and 5.2). Heavier primaries lose energy in spallation processes, thus reducing and hiding their production horizon (Section 5.1.1). They are also distinctly deflected due to magnetic fields along their path (Section 5.1.2). On the other hand, we have a useful and usable but not entirely convincing indication on the UHECR anisotropy in the Cen A data, supplemented by the time-reduced signal traced in the AGN sample (Section 5.3). In a sense, these as well as other analyses show what directional information can be gained without knowing the details of the propagation for unknown species of cosmic rays.

Our aim was to examine outputs received with models employed in searches for a directional association of extremely energetic CR events with their potential sources. Notwithstanding the relevance of such models, we utilized their parameters in order to make predictions for investigated signals, specify signal changes in subsequently collected data and compare different observations, while avoiding their retesting. Least affected implications were assured within the Bayesian framework by using a probability function for the source intensity, given the data, along with other kinds of prior inputs, if available. This scheme allows us to expand the range of results attainable in the classical analysis, refine data interpretation and address specific situations through naturally incorporating measurement uncertainties.

The feasibility of such an approach was backed up by our long-term focus on the arrival directions of the highest energy CRs. For example, we examined a set of PAO events pointing to the vicinity of Cen A [P02] and defined the properties of the observed signal. In a similar manner, we studied signals from the direction of the Virgo Cluster [P03], the Fornax Cluster [P04] and the supergalactic plane [P05]. It is also worth mentioning our first attempts in which gamma-ray bursts were examined as candidates to produce CRs [P01, P06] and searches for intrinsic anisotropy in the directional data [P23, P24]. We further investigated the most promising signal above background registered at the PAO from the direction of Cen A [P07, P08, P10], see also Refs. [24, 25]. Based on these findings, we paid special attention to the mass composition of primaries with arrival directions pointing to the vicinity of Cen A [P11, P12, P13, P14, P15]. We also investigated possible modification of the Cen A signal at lower energies for low-mass small charged species [P17, P20, P21], see also Ref. [92]. We studied the time evolution of the Cen A signal [P09, P19, P30] and compared it to the time evolution of the signal from nearby AGNs [P18, P22, P28]. Promising methods suitable for exploring directional data and for assessing the stability of source fluxes were presented at conferences [C03, C04, C08, C09, C10].

In our initial study [B01], the main focus was to record the knowledge of the strength of a predefined source, given the on-off data, while respecting their uncertainties. We proposed a new type of Bayesian solution to the on-off problem and summarized its most important features. The basic ingredient was the difference between unknown means of the source and background intensities. According to Jeffrey's two-dimensional premise for the on-off experiment, but unlike in other approaches, we considered underlying on- and off-source processes to be independent. The mean on- and off-source intensities were modeled using an adequately large class of conjugate distributions for the Poisson process. We obtained a nontrivial solution for the posterior distribution of the source intensity and discussed its usefulness.

Our main results can be summarized as follows. We were able to consistently describe the excess or deficit of events regardless of whether they occur in the source or background zone, as it is common in conventional treatments [93, 94]. Besides other suitable features, our method provides solutions in the case of small numbers, including the null experiment or the experiment with no background, when classical

methods are not easily applicable [93, 94, 95]. There are no problems with the discreteness of counting experiments or with unphysical estimates [96, 97, 98]. Using simplifying assumptions, we presented several analytic solutions showing the extent to which other results [99, 100, 101, 102, 103, 104] are included in our approach. On the other hand, we criticized some arguments and procedures used in previous studies [103, 104, 105]. Finally, we presented several numerical examples that may serve as guides for practical applications. The robustness of Bayesian inference was demonstrated in Monte Carlo examples. We showed results for very-high energy photons observed by the VERITAS setup [106] and by the *Fermi*-LAT [107] during or shortly after gamma-ray bursts, and assessed which of these observations can be associated with their optical counterparts. In most cases, when little is known about investigated phenomena, it turned out that commonly taken uninformative options are well suited for storing knowledge gained from on-off measurements.

In our subsequent study [B02], we focused on the specificities of CR data. In addition to the on-off difference [B01], we treated further two closely related variables that express the relative strength of the source with respect to the background. Namely, we considered the ratio of the source and background intensities and the fraction of the total intensity registered in the on-source zone. We presented relevant Bayesian solutions for these variables, identified previous approaches [100, 101, 108] included in our treatment and, relying on a solid statistical basis, we justified their role in analyzing directional data.

The main results include the following. First, we showed how observation-based information stored in the posterior distributions of fractional variables is advantageously utilized for the predictions of subsequent observations, given actual data. Second, backed by details of detection, we propose how to quantify disparities between different on-off measurements, focusing on the quantification of signal stability. It is worth noting that such predictions and comparison are not readily available within the classical treatment. Finally, we presented examples taken from CR physics. We examined the sets of data comprising time-growing numbers of the highest energy events collected in successive measurements at the PAO. In particular, the posterior outputs accessible in our Bayesian approach for AGN [22, 23, 24, 25] and Cen A [24, 25] hypotheses were summarized. Based on the actual data, we discussed the waiting times for a certain number of AGN or Cen A events that should be recorded in follow-up observations. We took information on the AGN signals observed in different periods of data collection and compared their strength between each other through their posterior distributions. More importantly, we also dealt with directional outputs collected in different experiments. Specifically, we demonstrated how to statistically assess the disparity between the strength of the AGN signal captured at the PAO [22, 23, 24, 25] and the strength of the signal detected from a source that should be responsible for the excess in directional data observed by the Telescope Array in the northern hemisphere [109].

6 Summary and outlook

In this thesis, I specified my own contribution to issues that are encountered when exploring the properties of cosmic rays at the highest energies. I included these contributions in the broader framework of current knowledge of the type and origin of cosmic particles and outlined their usefulness. This particular research, inspired by the Pierre Auger experiment, was developed in collaboration with several of my colleagues. Most of the proposed methods were tested on the data collected at the Pierre Auger Observatory, where they were also presented and discussed, supporting thus several collaborative publications at various stages of preparation.

In summary, we showed that the dispersion of mass in primary cosmic ray beams can be estimated with the help of various types of signals induced by extensive air showers [A01]. Concerning fluorescence data, we proposed a method of determining the primary mass composition based on the principle of maximum entropy backed by a simple shower model [A02]. In a Bayesian setting, we proposed a method for recording directional signals submerged in background [B01, B02]. This strategy was pursued with the view to revise our knowledge of preselected sources in subsequent measurements, make predictions for their activities and compare their manifestations.

The Pierre Auger Observatory is planned to operate until the end of 2024. The rich experimental material will be extended by precise measurements with the main ambition to distinguish various secondaries present in extensive air showers. The follow-up studies that will use new high-statistics data should provide better information about primary beams of cosmic particles and shower physics. They should ultimately help in understanding the world of hadronic interactions at extreme energies. Another challenging issue will be to clarify the existence of extremely energetic neutrinos and photons that could accompany some violent processes in the universe. Supported by outputs from these themes and by other observations, especially from high-energy gamma-ray astronomy, planned measurements and analyses are strongly believed to meet the main expectations. The new directional data supplemented with mass information should have the potential to delimit processes responsible for producing cosmic particles with the highest energy. They should also help to explore the impact of radiation and magnetic fields on the propagation of cosmic particles through the space, thus clarifying the prospects for charged particle astronomy.

Acknowledgments

I am indebted to many individuals over the years for contributing to my understanding of the highest energy cosmic rays. Throughout the work on the Auger project, I felt strongly supported by my colleagues and students in the Institute of Particle and Nuclear Physics and by my co-workers involved in the Auger experiment in the Institute of Physics of the Czech Academy of Sciences. In particular, I thank Jan Řídky who introduced me to the mystery of cosmic rays, and Petr Trávníček with whom I spent a lot of time while trying to figure something out. I would like to express my thanks to my co-authors, to Jana Nosková, Jakub Vícha, Petr Trávníček and Jan Ebr. The papers included in this thesis would not have been conceivable without their encouragement and input. Finally, I would like to acknowledge and thank our colleagues from the Pierre Auger Observatory for many helpful discussions and, especially, for the tremendous work with data, its analysis and interpretation from which I greatly benefit.

This work was supported by several grants of the Ministry of Education, Youth and Sports of the Czech Republic, currently by grants LTT18004 and LM2015038, and also by the Czech Science Foundation grant 14-17501S.

References

[1] M.Nagano, A.A.Waston, Rev.Mod.Phys. 72 (2000) 689.

[2] A.Letessier-Selvon, T.Stanev, Rev.Mod.Phys. 83 (2011) 907.

[3] K.-H.Kampert, M.Unger, Astroparticle physics 35 (2012) 660.

[4] K.Kotera, A.V.Olinto, Annu.Rev.Astron.Astrophys. 49 (2011) 119.

[5] A.A.Watson, Rep.Prog.Phys. 77 (2014) 036901.

[6] B.R.Dawson, M.Fukushima, P.Sokolsky, Prog.Theor.Exp.Phys. 2017(12) (2017) 12A101.

[7] F.Fenu for the Pierre Auger Collaboration, 35th International Cosmic Ray Conference, Busan, Korea, 12-20 July 2017, PoS(ICRC2017)486.

[8] J.N.Mathews for the Telescope Array Collaboration, 35th International Cosmic Ray Conference, Busan, Korea, 12-20 July 2017, PoS(ICRC2017)1096.

[9] J.Tsunesada *et al.*, 35th International Cosmic Ray Conference, Busan, Korea, 12-20 July 2017, PoS(ICRC2017)535.

[10] K.Greisen, Phys.Rev.Lett. 16 (1966) 748.

[11] G.T.Zatsepin, V.A.Kuzmin, JETP Lett. 4 (1966) 78.

[12] V.S.Berezinsky, S.I.Grigorieva, Astronomy & Astrophysics 199 (1988) 1.

[13] V.Berezinsky, A.Gazizov, S.Grigorieva, Phys.Rev. D 74, 2006, 043005.

[14] R.Aloisio, V.Berezinsky, A.Gazizov, Astroparticle physics 39-40 (2012) 129.

[15] D.Allard, Astroparticle physics 39-40 (2012) 33.

[16] A.M.Taylor, Astroparticle physics 54 (2014) 48.

[17] P.Abreu *et al.* [Pierre Auger Collaboration], Phys.Rev.Lett. 109 (2012) 062002.

[18] A.Aab *et al.* [Pierre Auger Collaboration], Phys.Rev.Lett. 117 (2016) 192001.

[19] A.Aab *et al.* [Pierre Auger Collaboration], Phys.Rev. D 91 (2015) 032003, Phys.Rev. D 91 (2015) 059901.

[20] A.Aab *et al.* [Pierre Auger Collaboration], Journal of Cosmology and Astroparticle Physics 04 (2017) 009.

[21] A.Aab *et al.* [Pierre Auger Collaboration], Phys.Rev. D 91 (2015) 092008.

[22] J.Abraham *et al.* [Pierre Auger Collaboration], Science 318 (2007) 938.

[23] J.Abraham *et al.* [Pierre Auger Collaboration], Astroparticle physics 29 (2008) 188.

[24] P.Abreu *et al.* [Pierre Auger Collaboration], Astroparticle physics 34 (2010) 314.

[25] A.Aab *et al.* [Pierre Auger Collaboration], Astrophysical Journal 804 (2015) 15.

[26] A.Aab *et al.* [Pierre Auger Collaboration], Journal of Cosmology and Astroparticle Physics 06 (2017) 026.

[27] A.Aab *et al.* [Pierre Auger Collaboration], Science 357 (2017) 1266.

[28] J.Abraham *et al.* [Pierre Auger Collaboration], Nuclear Instruments and Methods in Physics Research A 523 (2004) 50.

[29] A.Aab *et al.* [Pierre Auger Collaboration], Nuclear Instruments and Methods in Physics Research A 798 (2015) 172.

[30] D.Martello for the Pierre Auger Collaboration, 35th International Cosmic Ray Conference, Busan, Korea, 12-20 July 2017, PoS(ICRC2017)383.

[31] R.Smida for the Pierre Auger Collaboration, 35th International Cosmic Ray Conference, Busan, Korea, 12-20 July 2017, PoS(ICRC2017)390.

[32] J.M.Figueira for the Pierre Auger Collaboration, 35th International Cosmic Ray Conference, Busan, Korea, 12-20 July 2017, PoS(ICRC2017)396.

[33] E.M.Holt for the Pierre Auger Collaboration, 35th International Cosmic Ray Conference, Busan, Korea, 12-20 July 2017, PoS(ICRC2017)492.

[34] R.Gaior for the Pierre Auger Collaboration, M.Richardson, 35th International Cosmic Ray Conference, Busan, Korea, 12-20 July 2017, PoS(ICRC2017)372.

[35] P.Abreu *et al.* [Pierre Auger Collaboration], Journal of Instrumentation 8 (2013) P04009.

[36] J.Blazek for the Pierre Auger Collaboration, 35th International Cosmic Ray Conference, Busan, Korea, 12-20 July 2017, PoS(ICRC2017)362.

[37] M.Unger *et al.*, Nuclear Instruments and Methods in Physics Research A 588 (2008) 433.

[38] J.Abraham *et al.* [Pierre Auger Collaboration], Nuclear Instruments and Methods in Physics Research A 620 (2010) 227.

[39] A.Aab *et al.* [Pierre Auger Collaboration], Phys.Rev. D 90 (2014) 122005.

[40] K.Kamata, J.Nishimura, Prog.Theor. (Proc.Suppl.) 6 (1958) 93.

[41] K.Greisen, Ann.Rev.Nucl.Part.Sci. 10 (1960) 63.

[42] A.Aab *et al.* [Pierre Auger Collaboration], Journal of Cosmology and Astroparticle Physics 08 (2014) 019.

[43] C.Bonifazi, Nucl.Phys. B (Proc.Suppl.) 190 (2009) 20.

[44] A.Aab *et al.* [Pierre Auger Collaboration], Phys.Rev. D 90 (2014) 012012; Phys.Rev. D 90 (2014) 039904; Phys.Rev. D 92 (2015) 019903.

[45] A.Aab *et al.* [Pierre Auger Collaboration], Phys.Rev. D 93 (2016) 072006.

[46] A.Aab *et al.* [Pierre Auger Collaboration], Phys.Rev. D 96 (2017) 122003.

[47] J.Carlson, J.Oppenheimer, Phys.Rev. 51 (1937) 220.

[48] W.Heitler, International Series of Monographs on Physics, Oxford: Clarendon, 1954, 3rd ed.

[49] J.Alvarez-Muniz *et al.*, Phys.Rev. D 66 (2002) 033011.

[50] J.Matthews, Astroparticle physics 22 (2005) 387.

[51] J.R.Hörandel, Mod.Phys.Lett. A 22 (2007) 1533.

[52] R.Engel, D.Heck, T.Pierog, Ann.Rev.Nucl.Part.Sci. 61 (2011) 467.

[53] R.Ulrich, R.Engel, M.Unger, Phys.Rev. D 83 (2011) 054026.

[54] R.D.Parsons, C.Bleve, S.S.Ostapchenko, J.Knapp, Astroparticle physics 34 (2011) 832.

[55] E.Barcikowski, *et al.*, EPJ Web of Conferences 53 (2013) 01006.

[56] R.Abasi, *et al.*, JPS Conf.Proc. 9 (2016) 010016.

[57] V.de Souza, for the Pierre Auger Collaboration and the Telescope Array Collaboration, 35th International Cosmic Ray Conference, Busan, Korea, 12-20 July 2017, PoS(ICRC2017)522.

[58] J.Bellido for the Pierre Auger Collaboration, 35th International Cosmic Ray Conference, Busan, Korea, 12-20 July 2017, PoS(ICRC2017)506.

[59] S.Ostapchenko, Phys.Rev. D 83 (2011) 014018.

[60] T.Pierog, K.Werner, Phys.Rev.Lett. 101 (2008) 171101.

[61] T.Pierog, K.Werner, Phys.Rev. C 92 (2015) 034906.

[62] E.J.Ahn, *et al.*, Phys.Rev. D 80 (2009) 094003.

[63] D.d'Enterria *et al.*, Astroparticle physics 35 (2011) 98.

[64] M.Unger for the Pierre Auger Collaboration, 35th International Cosmic Ray Conference, Busan, Korea, 12-20 July 2017, PoS(ICRC2017)1102.

[65] P.Abreu *et al.* [Pierre Auger Collaboration], Journal of Cosmology and Astroparticle Physics 02 (2013) 026.

[66] A.Aab *et al.* [Pierre Auger Collaboration], Phys.Lett. B 762 (2016) 288.

[67] A.Aab *et al.* [Pierre Auger Collaboration], Phys.Rev. D 90 (2014) 122006.

[68] E.T.Jaynes, Phys.Rev. 106 (1957) 620.

[69] E.T.Jaynes, Phys.Rev. 108 (1957) 171.

[70] R.C.Rao, Linear Statistical Inference and Its Applications, John Willey & Sons, 1973.

[71] S.Pressé, *et al.*, Rev.Mod.Phys. 85 (2013) 1115.

[72] J.W.Cronin, Proceedings of TAUP 2003, [arXiv:astro-ph/0402487].

[73] D.Harari, S.Mollerach, E.Roulet, Journal of Cosmology and Astroparticle Physics 11 (2006) 012.

[74] R.Jansson, G.R.Farrar, Astrophysical Journal 757 (2012) 14.

[75] A.M.Hillas, Ann.Rev.Astr.Astrophys. 22 (1984) 425.

[76] J.Abraham *et al.* [Pierre Auger Collaboration], Phys.Rev.Lett. 101 (2008) 061101.

[77] J.Abraham *et al.* [Pierre Auger Collaboration], Phys.Lett. B 685 (2010) 239.

[78] W.Hanlon *et al.*, 35th International Cosmic Ray Conference, Busan, Korea, 12-20 July 2017, PoS(ICRC2017)536.

[79] T.Stroman, D.Bergman, 35th International Cosmic Ray Conference, Busan, Korea, 12-20 July 2017, PoS(ICRC2017)538.

[80] B.R.Dawson *et al.*, EPJ Web of Conferences 53 (2013) 01005.

[81] V.Verzi, *et al.*, JPS Conf.Proc. 9 (2016) 010001.

[82] D.Ivanov for the Pierre Auger Collaboration and the Telescope Array Collaboration, 35th International Cosmic Ray Conference, Busan, Korea, 12-20 July 2017, PoS(ICRC2017)498.

[83] R.Aloisio, V.Berezinsky, A.Gazizov, Astroparticle physics 34 (2011) 620.

[84] W.D.Apel *et al.*, Astroparticle physics 47 (2013) 54.

[85] M.Unger, G.R.Farrar, L.A.Anchordoqui, Phys.Rev. D 92 (2015) 123001.

[86] N.Globus, D.Allard, E.Parizot, Phys.Rev. D 92 (2015) 021302(R).

[87] A.Aab *et al.* [Pierre Auger Collaboration], Journal of Cosmology and Astroparticle Physics 04 (2017) 038.

[88] M.P.Véron–Cetty, and P. Véron, Astronomy & Astrophysics 455 (2006) 773.

[89] J.Abraham *et al.* [Pierre Auger Collaboration], Astroparticle physics 27 (2007) 244.

[90] U.Giaccari for the Pierre Auger Collaboration, 35th International Cosmic Ray Conference, Busan, Korea, 12-20 July 2017, PoS(ICRC2017)483.

[91] A.Aab *et al.* [Pierre Auger Collaboration], Astrophysical Journal Letters 853:L29, 2018.

[92] P.Abreu *et al.* [Pierre Auger Collaboration], Journal of Cosmology and Astroparticle Physics 06 (2011) 022.

[93] T.P.Li, Y.Q.Ma, Astrophysical Journal 272 (1983) 317.

[94] R.D.Cousins, J.T.Linnemann, J.Tucker, Nuclear Instruments and Methods in Physics Research A 595 (2008) 480.

[95] G.Cowan, K.Cranmer, E.Gross, O.Vitells, European Physical Journal C 71 (2011) 1554; and C 73 (2011) 2501.

[96] G.J.Feldman, R.D.Cousin, Phys.Rev. D 57 (1998) 3873.

[97] R.D.Cousins, Nuclear Instruments and Methods in Physics Research A 417 (1998) 391.

[98] W.A.Rolke, A.M.López, J.Conrad, Nuclear Instruments and Methods in Physics Research A 551 (2005) 493.

[99] O.Helene, Nuclear Instruments and Methods 212 (1983) 319.

[100] O.Helene, Nuclear Instruments and Methods 228 (1984) 120.

[101] H.B.Prosper, Nuclear Instruments and Methods in Physics Research A 241 (1985) 236.

[102] H.B.Prosper, Phys.Rev. 37 (1988) 1153.

[103] P.Gregory, Bayesian Logical Data Analysis for the Physical Sciences, Cambridge, Cambridge University Press, 2005, Chapter 14.

[104] M.L.Knoetig, Astrophysical Journal 790 (2014) 106.

[105] D.Casadei, Astrophysical Journal 798 (2015) 5.

[106] V.A.Acciari *et al.*, Astrophysical Journal 743 (2011) 62.

[107] A.A.Abdo *et al.*, Astrophysical Journal 707 (2009) 580.

[108] S.Gillesen, H.L.Harney, Astronomy & Astrophysics 430 (2005) 355.

[109] K.Kawata *et al.* for the Telescope Array Collaboration, 34th International Cosmic Ray Conference, The Hague, The Netherlands, 30 July - 6 August 2015, PoS(ICRC2015)276.

Author's Publications

[A01] J.Vicha, P.Travnicek, D.Nosek, J.Ebr, Study of dispersion of mass distribution of ultra-high energy cosmic rays using a surface array of muon and electromagnetic detectors, Astroparticle Physics 69, 11-17, 2015.

[A02] D.Nosek, J.Ebr, J.Vicha, P.Travnicek, J.Noskova, Maximum entropy analysis of cosmic ray composition, Astroparticle Physics 76, 9-18, 2016.

[B01] D.Nosek, J.Noskova, On Bayesian analysis of on-off measurements, Nuclear Instruments and Methods in Physics Research A 820, 23-33, 2016.

[B02] D.Nosek, J.Noskova, A Bayesian on-off analysis of cosmic ray data, Nuclear Instruments and Methods in Physics Research A 867, 222-230, 2017.

Conference Contributions by the Author

[C01] J.Ridky, D.Nosek, On Sensitivity of Cherenkov Radiation to the Dynamics of High Energy Cosmic Ray Interactions, 8th International Workshop on Topics in Astroparticle and Underground Physics, Seattle, WA, USA, September 05-09, 2003, Nucl.Phys. B (Proc.Suppl.) 138 (2005) 299.

[C02] J.Ridky, D.Nosek, P.Travnicek, P.Necesal, Prompt muons in extended air showers, 30th International Cosmic Ray Conference, Merida, Mexico, 3-11 July 2007, Vol.4 (HE part 1), 605.

[C03] D.Nosek, J.Noskova, Order statistics of the arrival directions of the highest energy cosmic rays, 31th International Cosmic Ray Conference, Lodz, Poland, 7-15 July 2009,
http://icrc2009.uni.lodz.pl/proc/pdf/icrc0923.pdf

[C04] D.Nosek, S.Stefanik, J.Noskova, Testing time variability of gamma-ray flux, 33th International Cosmic Ray Conference, Rio de Janeiro, Brasil, 2-9 July 2013, icrc2013-0120, ISBN 978-85-61516-15-4, [arXiv:1309.6476].

[C05] D.Nosek, J.Vicha, J.Noskova, J.Ebr, Testing chemical composition of highest energy cosmic rays, 33th International Cosmic Ray Conference, Rio de Janeiro, Brasil, 2-9 July 2013, icrc2013-0472, ISBN 978-85-61516-15-4, [arXiv:1309.5924].

[C06] J.Vicha, P.Travnicek, D.Nosek, J.Ebr, On the methods to determine signal attenuation curve for different surface arrays, 33th International Cosmic Ray Conference, Rio de Janeiro, Brasil, 2-9 July 2013, icrc2013-1068, ISBN 978-85-61516-15-4, [arXiv:1310.0330].

[C07] J.Vicha, P.Travnicek, D.Nosek, J.Ebr, Signal Attenuation Curve for Different Surface Detector Arrays, Proceedings of the 14th ICATPP Conference, Como, Italy, 23-27 September 2013, Astroparticle, Particle, Space Physics, Radiation Interaction, Detectors and Medical Physics Applications 8, 2014, 162, [arXiv:1408.1595].

[C08] S.Stefanik and D.Nosek, Variability of VHE gamma-ray sources, Frontier Research in Astrophysics Workshop, Mondello, Italy, May 26-31, 2014, Nucl.Phys. B (Proc.Suppl.) 256-257 (2014) 258.

[C09] S.Stefanik, D.Nosek, Variability of VHE gamma-ray emission from the binary PSR B1259-63/LS 2883, Conference on Searching for the Sources of Galactic Cosmic Rays (SuGAR), Geneva, Switzerland, January 21-23, 2015, EPJ Web of Conferences 105 (2015) 04006.

[C10] D.Nosek, S.Stefanik, J.Noskova, Significance for signal changes in gamma-ray astronomy, 34th International Cosmic Ray Conference, The Hague, The Netherlands, 30 July - 6 August 2015, PoS(ICRC2015)710, [arXiv:1509.00353].

[C11] J.Vicha, P.Travnicek and D.Nosek, On the Combined Analysis of Muon Shower Size and Depth of Shower Maximum, 34th International Cosmic Ray Conference, The Hague, The Netherlands, 30 July - 6 August 2015, PoS(ICRC2015)433, [arXiv:1509.06320].

[C12] J.Vicha, D.Nosek, P.Travnicek, J.Ebr, Mass Composition of Cosmic Rays with Combined Surface Detector Arrays, 35th International Cosmic Ray Conference, Busan, Korea, 12-20 July 2017, PoS(ICRC2017)482, [arXiv:1708.06164].

Internal GAP-Notes by the Author

[P01] M.Bohacova, J.Grygar, M.Hrabovsky, D.Mandat, D.Nosek, L.Nozka, M.Palatka, M.Pech, M.Prouza, J.Ridky, P.Schovanek, R.Smida, P.Travnicek, Cosmic rays from GRBs and SGR 1806-20, GAP-2006-69.

[P02] D.Nosek, J.Noskova, An excess of the highest energy Auger events in the region around Centaurus A, GAP-2009-51.

[P03] D.Nosek, J.Noskova, On a deficit of the most energetic Auger events in the direction of Virgo A, GAP-2009-52.

[P04] D.Nosek, J.Noskova, Planar structure of the highest energy Auger events near the supergalactic plane, GAP-2009-56.

[P05] D.Nosek, J.Noskova, On an absence of the most energetic Auger events in the direction of Fornax A, GAP-2009-59.

[P06] R.Smida, J.Grygar, D.Nosek, Update of coincidences between gamma-ray bursts and cosmic ray events measured till April 2009, GAP-2009-64.

[P07] D.Nosek, J.Noskova, An excess of the highest energy Auger events in the region around Centaurus A - And yet it shines, GAP-2009-145.

[P08] D.Nosek, J.Noskova, An excess of the highest energy Auger events in the region around Centaurus A - 27 published events, GAP-2009-148.

[P09] D.Nosek, J.Noskova, A remark on the arrival time distribution of the highest energy Auger events, GAP-2009-151.

[P10] D.Nosek, J.Noskova and P.Travnicek, Energy spectrum of Auger events pointing in the vicinity of Centaurus A, GAP-2009-178.

[P11] D.Nosek, J.Noskova, P.Travnicek, M.Nyklicek, Heavy cosmic ray primaries from the region around Centaurus A, GAP-2010-007.

[P12] D.Nosek, J.Noskova, P.Travnicek, An excess of deeply penetrating cosmic ray shower in the vicinity of Centaurus A, GAP-2010-023.

[P13] D.Nosek, J.Noskova, P.Travnicek, An image of the region around Centaurus A on the Auger sky of deeply penetrating showers, GAP-2010-026.

[P14] M.Nyklicek, P.Travnicek, D.Nosek, Monte-Carlo studies of the composition of cosmic rays comming from the region around Centaurus A, GAP-2010-039.

[P15] D.Nosek, J.Noskova, P.Travnicek, On anisotropy and chemical composition in the direction of Centaurus A, GAP-2010-079.

[P16] D.Nosek, J.Noskova, On-off analysis in cosmic ray physics, GAP-2010-085.

[P17] D.Nosek, J.Noskova, Can we expect low-energy anisotropy in the direction of Centaurus A?, GAP-2010-086.

[P18] D.Nosek, J.Noskova, What happened to the AGN signal?, GAP-2010-088.

[P19] D.Nosek, J.Noskova, A note on the evolution of anisotropy in the vicinity of Centaurus A, GAP-2010-089.

[P20] D.Nosek, J.Noskova, Low-energy anisotropy toward Centaurus A, GAP-2011-016.

[P21] D.Nosek, J.Noskova, Toward a better understanding of low–energy anisotropy around Centaurus A, GAP-2011-020.

[P22] D.Nosek, J.Noskova, No excess signal from ANGs, GAP-2011-022.

[P23] D.Nosek, J.Noskova, Intrinsic anisotropy of the highest energy Auger events, GAP-2011-024.

[P24] D.Nosek, J.Noskova, Intrinsic anisotropy at low energies, GAP-2011-027.

[P25] J.Vicha, P.Travnicek, D.Nosek, SD to FD energy ratio as parameter sensitive to muon content, GAP-2011-042.

[P26] D.Nosek, J.Ebr, J.Vicha, J.Noskova, Decomposition of the mass composition, GAP-2013-061.

[P27] D.Nosek, J.Ebr, J.Vicha, P.Travnicek, J.Noskova, Partition analysis of primary mass composition, GAP-2015-053.

[P28] D.Nosek, J.Noskova, On signals from AGNs, GAP-2015-095.

[P29] J.Vicha, P.Travnicek, D.Nosek, Interpretation of dependence of mean ground signal on depth of shower maximum, GAP-2016-001.

[P30] D.Nosek, S.Stefanik, J.Noskova, The case of Centaurus A, GAP-2016-046.

A Study of dispersion of mass distribution

J.Vicha, P.Travnicek, D.Nosek, J.Ebr, *Study of dispersion of mass distribution of ultra-high energy cosmic rays using a surface array of muon and electromagnetic detectors*, Astroparticle Physics 69, 11-17, 2015 [arXiv:1503.07734].
DOI: 10.1016/j.astropartphys.2015.03.004

B Maximum entropy analysis of cosmic ray composition

D.Nosek, J.Ebr, J.Vicha, P.Travnicek, J.Noskova, *Maximum entropy analysis of cosmic ray composition*, Astroparticle Physics 76, 9-18, 2016 [arXiv:1512.09248].
DOI: 10.1016/j.astropartphys.2015.12.005

C On Bayesian analysis of on-off measurements

D.Nosek, J.Noskova, *On Bayesian analysis of on-off measurements*, Nuclear Instruments and Methods in Physics Research A 820, 23-33, 2016 [arXiv:1603.03386]. DOI: 10.1016/j.nima.2016.02.094

D A Bayesian on-off analysis of cosmic ray data

D.Nosek, J.Noskova, *A Bayesian on-off analysis of cosmic ray data*, Nuclear Instruments and Methods in Physics Research A 867, 222-230, 2017 [arXiv:1707.03155]. DOI: 10.1016/j.nima.2017.06.034